



저작자표시-비영리-변경금지 2.0 대한민국

이용자는 아래의 조건을 따르는 경우에 한하여 자유롭게

- 이 저작물을 복제, 배포, 전송, 전시, 공연 및 방송할 수 있습니다.

다음과 같은 조건을 따라야 합니다:



저작자표시. 귀하는 원저작자를 표시하여야 합니다.



비영리. 귀하는 이 저작물을 영리 목적으로 이용할 수 없습니다.



변경금지. 귀하는 이 저작물을 개작, 변형 또는 가공할 수 없습니다.

- 귀하는, 이 저작물의 재이용이나 배포의 경우, 이 저작물에 적용된 이용허락조건을 명확하게 나타내어야 합니다.
- 저작권자로부터 별도의 허가를 받으면 이러한 조건들은 적용되지 않습니다.

저작권법에 따른 이용자의 권리는 위의 내용에 의하여 영향을 받지 않습니다.

이것은 [이용허락규약\(Legal Code\)](#)을 이해하기 쉽게 요약한 것입니다.

[Disclaimer](#)

Molecular basis for dynamic change in the ion selectivity of anion channels

Ikhyun Jun

Department of Medical Science

The Graduate School, Yonsei University

Molecular basis for dynamic change in the ion selectivity of anion channels

Directed by Professor Min Goo Lee

The Doctoral Dissertation
submitted to the Department of Medical Science,
The Graduate School of Yonsei University
in partial fulfillment of the requirements for the degree of
Doctor of Philosophy

Ikhyun Jun

December 2016

This certifies that the Doctoral
Dissertation of Ikhyun Jun is approved.

Thesis Supervisor: Min Goo Lee

Thesis Committee Member #1: Chul Hoon Kim

Thesis Committee Member #2: Eung Kweon Kim

Thesis Committee Member #3: Jae Young Choi

Thesis Committee Member #4: Joo Young Kim

The Graduate School
Yonsei University

December 2016

ACKNOWLEDGEMENTS

박사 학위 과정을 진행하며 많은 분들에게서 저를 이끌어 주고 지지해 주셔서 이 과정을 무사히 마칠 수 있었습니다. 평소에 감사하다는 말씀을 드리지 못하였는데 지면을 통해서나마 감사인사를 드리고자 합니다. 먼저 학위 과정 동안 저에게 애정 어린 가르침을 주시고 언제나 본받아야 할 모습을 보여 주신 저의 지도교수님 이신 이민구교수님께 진심으로 감사드립니다. 교수님께 지식적인 배움만이 아니라 저의 인격적인 성장 및 나아갈 길을 보여주셨습니다. 또한 바쁘신 와중에도 학위 논문을 검토해 주시고 격려와 축하를 보내주신 김응권 교수님, 김철훈 교수님, 최재영 교수님, 김주영 교수님께 감사 드립니다. 또한 약리학교실에서 박사과정을 올바르게 나아갈 수 있도록 허락하고 지도해주신 김경환 교수님, 안영수 교수님, 김동구 교수님, 박경수 교수님, 김형범 교수님, 지현영 교수님께도 이 자리를 통해 감사 드립니다. 임상 수련을 받고 안과 전문의가 될 수 있도록 가르쳐 주시고 기초의학을 연구할 수 있는 길을 열어 주신 김응권 교수님, 서경률 교수님, 이형근 교수님, 김태임 교수님을 비롯하여, 이상열 교수님, 한승한 교수님, 김찬윤 교수님, 이승규 교수님 및 모든 안과학교실 교수님께 진심으로 감사 드립니다.

5년 간의 박사 과정 동안 함께 생활하며 즐거운 시간을 함께 하고 힘든 시간 서로를 위로하며 많은 도움을 주신 약리학 교실 선, 후배님 및 동료들, 민선자 선생님, 임종수 선생님께 감사 드립니다. 제가 연구실에 처음 와서 아무 것도 모를 때 사수로서 하나부터 열까지 꼼꼼하게 가르쳐 주고 응원해 준 진세형, 언제나 절 챙겨주고 모자란 부분을 채워준 김연정 선생님, 언제나 즐겁게 생활할 수 있게 해주고 절 많이 아껴주신 형순이 형, 은석이 형, 친 누나처럼 저를 아껴준 정남 누나, 신혜 누나, 많은 것을 가르쳐 주고 도와 준 우영이, 준희, 연구실 동기로 함께 한 수민이, 함께 연구실에서 늦게 까지 시간을 보낸 한상이, 지윤이, 정우, 학이,



운이, 소원이, 준석이, 경지, 초예, 영익이, 세영이, 윤진이, 함께 연구를 하면서 많은 가르침을 주신 지현영 선생님, 남주현 선생님, 신동훈 선생님, 학부생이지만 대학원생 보다 더 열심히 저를 도와준 병규, 민지에게 감사한 마음을 전합니다. 또한 저와 함께 Physician-Scientist를 시작하고 누구보다 저의 마음을 이해하고 서로 서로 지탱하며 동고 동락 한 준원이, 태균이, 형진이 형, 다함이 에게 감사하고, 우리 세가지 소원 친구들, 대현이, 동물이, 근영이, 경록이, 원택이, 연익이, 시형이 에게도 고맙다는 말을 전합니다.

언제나 응원해 주시고, 격려해 주시고, 저를 위해 많은 것을 아끼지 않고 내어 주시는 사랑하는 부모님, 장인어른, 장모님께 진심으로 감사드립니다. 바쁘다는 핑계로 신경을 못 써준 동생 준호, 처남 네 가족들, 친할머니, 외할머니께도 고마운 마음을 전합니다. 마지막으로 제대로 챙겨주지도 못하고, 부족한 면도 많고, 여유를 갖지 못하는 저를 옆에서 지켜주고 항상 내 편이 되어 응원해주는 우리 아내, 지은이와 애교로 저의 피로를 풀어 주는 기특하고, 귀여운 우리 딸 서빈이와 아들 유찬이에게 참으로 고맙고 사랑한다는 말을 전합니다. 함께 모든 것을 이겨내며 아름답고 행복하게 살아 가겠습니다.

졸업은 끝이 아닌 새로운 시작을 의미합니다. 모든 분들께 받은 사랑과 감사를 새로운 시작과 함께 저를 이끌어나가는 원동력으로 삼아 더욱 발전하고 성장하는데 끊임없는 노력을 해 나가도록 하겠습니다. 다시 한번 감사 드립니다.

2016년 12월

TABLE OF CONTENTS

ABSTRACT	1
I. INTRODUCTION	3
II. MATERIALS AND METHODS	7
1. Cell Culture, and Plasmids.....	7
2. Immunoblotting.....	7
3. Electrophysiology in Cultured Cells.....	8
4. Calculation of Relative Ion Permeability (P_X/P_{Cl}), Dielectric Constant (ϵ), and Pore Size Calculation of Relative Ion Permeability (P_X/P_{Cl}), Dielectric Constant (ϵ), and Pore Size.....	10
5. Molecular Dynamics (MD) Simulations of GlyR Structure.....	12
6. Cortical Slice Preparation, Whole-Cell Recording, and GABA Puffing....	15
7. Modeling of P_X/P_{Cl} using Free Energy of Anions and Pore Diameter of Anion Channels.....	17
8. Statistical Analysis.....	18
III. RESULTS	20
1. The P_{HCO_3}/P_{Cl} Increases in CFTR and ANO1 Have an Interaction with Electric Permittivity and Pore Size.....	20
2. Pore Dilution Increases P_{HCO_3}/P_{Cl} and ϵ of GlyR by Increasing Water Occupancy in the Selectivity Filter Region.....	29
3. Increased HCO_3^- Efflux from GABA _A R Evokes Neuronal Excitation..	38
4. A Model to Predict Ion Selectivity of Anion Channels using Electric Permittivity and Pore size.....	44



IV. DISCUSSION.....	49
V. CONCLUSION.....	55
REFERENCES.....	56
ABSTRACT (IN KOREAN).....	62
PUBLICATIONS LIST.....	64

LIST OF FIGURES

Figure 1.	Anion Permeability of CFTR in Control Cells.....	23
Figure 2.	Anion Permeability of CFTR in WNK1/SPAK Activated Cells.....	24
Figure 3.	Anion Permeability of CFTR in Cells with Inactivated WNK1/SPAK.....	25
Figure 4.	Anion Permeability of CFTR in Control Cells at Low [Cl ⁻] _i	26
Figure 5.	Anion Permeability of CFTR in WNK1/SPAK- Depleted Cells.....	27
Figure 6.	Increased HCO ₃ ⁻ Permeability is Associated with Increases in Dielectric Constant (ε) and Pore Size in CFTR and ANO1.....	28
Figure 7.	Pore Dilation Increases P _{HCO₃} /P _{Cl} and ε of the Glycine Receptor (GlyR).....	31
Figure 8.	Molecular Dynamic (MD) Analyses of the GlyR Pore.....	32
Figure 9.	Pore Dilation Increases ε of GlyR by Increasing Water Occupancy in the Selectivity Filter Region...34	
Figure 10.	High-dose GABA Stimulation Increases P _{HCO₃} /P _{Cl} and ε of GABA _A R.....	40
Figure 11.	Increase HCO ₃ ⁻ Efflux through GABA _A R Evokes	

Neuronal Excitation.....42

Figure 12. The Pore Size and Thermodynamic Energy
Contribute to the Ion Selectivity of Anion
Channels.....45

Figure 13. An Illustrated Model for the Dynamic Increase of
 $P_{\text{HCO}_3}/P_{\text{Cl}}$ in Anion Channels.....48

LIST OF TABLES

Table 1.	Lennard-Jones (LJ) and Electrostatic Parameters Used in the Simulations.....	36
Table 2.	Comparison of Energy Barriers for Ion Transport across the Selectivity Filter Region Deduced from MD Calculations.....	37
Table 3.	Dielectric Constant (ϵ), Channel Pore Diameter (d), Threshold Ion Diameter (a_0), and Channel-Specific Weight Factor (α)	47

ABSTRACT

**Molecular basis for dynamic change
in the ion selectivity of anion channels**

Ikhyun Jun

*Department of Medical Science
The Graduate School, Yonsei University*

(Directed by Professor Min Goo Lee)

Ion permeation through anion channels plays essential roles in our body. However, how the anion channels retain ion selectivity and how the anion selectivity is regulated are largely unknown. Here, I show that the combined effects of thermodynamic hydration energy and size-exclusion force of the pore determine the anion selectivity. The dielectric constant increase and pore size enlargement are found when WNK1/SPAK associated HCO_3^- permeability increase happens in CFTR. In ANO1/TMEM16A channel, this finding is also found during HCO_3^- permeability change due to high intracellular calcium concentration. In GlyR, P-2' Δ mutation caused the pore dilation, HCO_3^- permeability change, and electric permittivity rise. Molecular dynamic simulation showed that pore dilation not only affected the energy barriers of size exclusion but that of ion dehydration by altering

water occupancy in the channel filter region. Application of high dose GABA dynamically modulated anion selectivity of GABA_AR, which is essential for GABA induced action potential generation in pyramidal neuron of sensorimotor cortex. New anion selectivity modeling was performed by integration of thermodynamic hydration energy and size-exclusion force of the pore. Importantly cellular stimuli dynamically modulated anion selectivity by changing pore size, and a finding that is common to all anion channels studied, including CFTR, ANO1/TMEM16A, GlyR, and GABA_AR, is that pore dilation increases $P_{\text{HCO}_3^-}/P_{\text{Cl}^-}$ by affecting energy barriers of size exclusion and ion dehydration of HCO_3^- permeation. I also provide evidence and suggest that the dynamic increase in $P_{\text{HCO}_3^-}/P_{\text{Cl}^-}$ is involved in many physiological and pathophysiological processes, such as CFTR-mediated epithelial HCO_3^- secretion and GABA_AR-evoked neuronal excitation.

Key words: anion selectivity, CFTR, ANO1, glycine receptor, gaba receptor, bicarbonate, dielectric constant, pore size

**Molecular basis for dynamic change
in the ion selectivity of anion channels**

Ikhyun Jun

*Department of Medical Science
The Graduate School, Yonsei University*

(Directed by Professor Min Goo Lee)

I. INTRODUCTION

Anion channels are essential for keeping the cells alive and mediating diverse functions. Although the ion selection mechanisms of cation channels are relatively well defined,¹ those of anion channels are still poorly understood. Anion channels are thought as Cl^- channels, because most abundant anion in the body is Cl^- . However, various other anions are also permeable to many anion channels. Usually, large halide ions, such as I^- and Br^- , are more permeable to many anion channels than Cl^- .²⁻⁴ The reason for this phenomenon is that large symmetrically charged ions have the small hydration/dehydration energy, and ions in general pass through the channel after dehydration. Accordingly, it was suggested that the pore of anion channels is comprised of a large polarizable tunnel, in that ion selectivity can

be determined by the electric permittivity.^{3,4} According to this concept, a fixed value of the dielectric constant (ϵ , relative permittivity) in the channel determines a specific condition of a certain anion channel and the selectivity of ions.³⁻⁵ However, increasing evidence suggests that ion selectivity is dynamically altered by cellular stimuli or strong agonist stimulations.^{6,7} Furthermore, some anion channels, such as CFTR, showed low permeability of the large halide ion I^- which is contradictory to the polarizable tunnel theory.⁸

And other determinant of ion selectivity is pore size of channel. Previous study revealed that alanine transition of threonine residue of transmembrane domain (TM) 6 of CFTR increased the permeability of several polyatomic anions.⁹ They found the pore size of CFTR increased by estimation. The deletion of proline 250 (P-2' Δ) of glycine receptor (GlyR) decreased the anion/cation permeability ration and increased the pore diameter.¹⁰ In addition, the permeability of bicarbonate, acetate, methanesulfonate and gluconate increased. This is also applicable to cation channels. In neuronal P2X receptor channel, longer ATP application more than 10 s made the channel permeable to larger cations like the propidium analog YO-PRO-1, and N-methyl-D-glucamine.¹¹

Although many anions are permeable to anion channels, Cl^- and HCO_3^- are the two most plentiful anions that are the major charge carrier of anion channels in animal cells. HCO_3^- permeation through anion channel plays many important roles ranging from epithelial fluid secretion to neuronal excitation.¹²⁻¹⁴ Epithelial cells in gastrointestinal system secrete HCO_3^- to saliva, intestinal fluids, and pancreatic juice. HCO_3^- in airway surface fluid secreted by respiratory epithelium has valuable roles. Fluids secreted by reproductive organs also contain high HCO_3^- . As a major component of the

$\text{CO}_2/\text{HCO}_3^-$ buffer system, HCO_3^- controls intracellular and extracellular pH, and guards toxic fluctuations of pH.¹⁵ Bicarbonate rich fluids secreted by pancreas and duodenum neutralize gastric acid and provide a suitable pH environment for the proper function of digestive enzymes in the intestine.¹⁶ In addition, bicarbonate acts as a moderate chaotropic ion, to facilitate the solubilization of macromolecules such as mucins.¹⁷ Inadequate epithelial bicarbonate secretion results in defective mucin hydration and solubilization,¹⁸ and causes hyper-viscous mucus that blocks ductal structures of the lung and pancreas.^{19,20} Therefore, abnormal HCO_3^- secretion is related to a wide spectrum of diseases in the gastrointestinal, respiratory, and genitourinary systems, including pancreatitis, cystic fibrosis, and infertility.^{14,20-22}

CFTR has important roles in bicarbonate secretion in epithelial cells. The mutation of CFTR can cause cystic fibrosis, which is one of most common lethal hereditary disease in western countries. Patients with cystic fibrosis secrete acidic pancreatic juice.²³ CFTR, located in apical membrane, secretes Cl^- into lumen according to the electrochemical gradient. The apical $\text{Cl}^-/\text{HCO}_3^-$ exchangers move HCO_3^- into lumen by recycling Cl^- .¹⁴ In addition, in certain situation when intracellular chloride concentration is low, the bicarbonate permeability of CFTR is dynamically increased by the protein kinase WNK1.⁷ It means the CFTR secretes HCO_3^- directly, which is important in condensing high bicarbonate in pancreatic fluid.

Moreover HCO_3^- permeation through $\text{GABA}_\text{A}\text{R}$ is associated with the paradoxical neuronal excitation by $\text{GABA}_\text{A}\text{R}$.^{12,24} In general, anion permeation through the glycine receptor (GlyR) and GABA_A receptor ($\text{GABA}_\text{A}\text{R}$) plays a principal function in inhibitory neurotransmission in

nervous system. Interestingly, an intensive GABA_AR stimulation paradoxically produces neuronal excitation, which may contribute to the generation of neuronal networks during early brain development as well as the pathological neuronal activity of epilepsy.²⁵

Accordingly, the $\text{HCO}_3^-/\text{Cl}^-$ permeability ratio ($P_{\text{HCO}_3}/P_{\text{Cl}}$) is an important parameter of anion channel function. Of interest, $P_{\text{HCO}_3}/P_{\text{Cl}}$ of anion channels can be modulated dynamically by various cellular stimuli. For example, activations of the WNK1/SPAK kinases and Ca^{2+} /calmodulin, respectively, have been shown to increase $P_{\text{HCO}_3}/P_{\text{Cl}}$ of CFTR and ANO1.^{6,7} In the present study, I aimed to identify the molecular basis of $P_{\text{HCO}_3}/P_{\text{Cl}}$ modulation by cellular stimuli and to further explore the basic mechanism of ion permeation through anion channels using an integrated molecular, physiological, and computational approach.

II. MATERIALS AND METHODS

1. Cell culture, and plasmids

The plasmids expressing Myc-rWNK1, Flag-mSPAK, hCFTR, and hANO1/TMEM16A have been previously described.^{6,7,26} Mammalian expressible pCMV-myc hGLRA1 plasmids were subcloned using PCR amplification of purchased cDNA of hGLRA1 from GE Dharmacon (Lafayette, CO, USA; Clone ID: 30915298). The hGlyR P-2' Δ mutant plasmid was generated with a PCR-based site-directed mutagenesis. Plasmids expressing $\alpha 1$ (pCIS2-h $\alpha 1$), $\beta 3$ (pCMV6-XL-h $\beta 3$), and $\gamma 2L$ (pCDNA3.1-h $\gamma 2L$) subunits of hGABA_AR were a kind gift from Dr. Neil Harrison at Columbia University, New York, NY, USA. The siRNAs against WNK1 and SPAK were purchased from GE Dharmacon (Lafayette, CO, USA; WNK1, SMARTpool L-005362-02-0005; SPAK, SMARTpool L-050614-00-0005). HEK 293T cells were maintained in Dulbecco's modified Eagle's medium (DMEM)-HG (Invitrogen, Carlsbad, CA, USA) supplemented with 10% (v/v) fetal bovine serum and penicillin (100 U/mL)/streptomycin (0.1 mg/ml). Plasmids were transiently transfected into HEK 293T cells using Lipofectamine Plus (Invitrogen) reagent. The plasmids expressing green fluorescence protein were co-transfected to confirm an average transfection rate over 90%.

2. Immunoblotting

Immunoblotting was performed as described previously.⁷ Transfected HEK 293T cells were washed three times with ice-cold phosphate-buffered saline (PBS) and harvested. The protein samples were recovered in a sodium dodecyl sulfate (SDS) buffer and separated by SDS-polyacrylamide gel electrophoresis. The separated proteins were transferred to a nitrocellulose membrane and blotted with appropriate primary and secondary antibodies. Protein bands were detected by enhanced chemiluminescence (GE Healthcare, Little Chalfont, UK). Antibodies against SPAK (no. 2281; Cell Signaling Technology, Danvers, MA, USA), WNK1 (ab53151; Abcam, Cambridge, MA, USA) and actin (sc-1616; Santa Cruz Biotechnology, Dallas, TX, USA) were obtained from commercial sources.

3. Electrophysiology in Cultured Cells

Whole-cell and outside-out patch clamp techniques were applied to measure the anion channel activities in HEK 293T cells as reported previously^{6,7,26} with minor modifications. Briefly, I transferred the cells into a bath mounted on a stage with an inverted microscope (IX-70, Olympus, Tokyo, Japan). To achieve the conventional whole-cell clamp, I formed a gigaseal and then ruptured the patch membrane. To perform outside-out excised patch clamp experiments, the electrode was slowly withdrawn from the whole-cell clamp state, allowing a bulb of the membrane to bleb out from the cell. This bleb was pulled away until it detached from the cell and reformed a convex membrane at the end of the pipet. The perfusion rate of

bath solution was 5 mL/min. The voltage and current recordings were performed at room temperature (22–25°C). Patch pipettes with a free-tip resistance of about 2–5 MΩ were connected to the head stage of a patch-clamp amplifier (Axopatch-700B, Molecular Devices, Sunnyvale, CA, USA). pCLAMP software v. 10.2 and Digidata-1440A (Molecular Devices) were used to obtain data and give command pulses. AgCl reference electrodes were applied to the bath via a 1.5% agar bridge containing 3 M KCl solution. Voltage and current traces were stored and analyzed using Clampfit v. 10.2 and Origin v. 8.0 (OriginLab Corp., Northampton, MA, USA). Currents were sampled at 5 kHz. All data were low-pass filtered at 1 kHz.

The standard pipette solution contained (in mM) 148 N-methyl-D-glucamine-Cl (NMDG-Cl), 1 MgCl₂, 3 MgATP, 10 HEPES, and 10 ethylene glycol tetraacetic acid (EGTA) (pH 7.2). The low Cl⁻-containing pipette solution contained (in mM) 140 NMDG-Gluconate, 8 HCl, 5 EGTA, 1 MgCl₂, 3 Mg-ATP, and 10 HEPES (pH 7.2). The standard bath solution contained (in mM) 146 NMGD-Cl, 1 CaCl₂, 1 MgCl₂, 5 glucose, and 10 HEPES (pH 7.4). In GlyR and GABA_AR experiments, NMDG⁺ was replaced with Na⁺ in the pipette and bath solutions. For permeability evaluations, 150 Cl⁻ in the bath solution was substituted with 146 X⁻ + 4 Cl⁻, where X is the substitute anion (F⁻, Br⁻, NO₃⁻, I⁻, HCO₃⁻, or gluconate⁻ in a form of NaX). The bath solutions containing an increased concentration of Cl⁻ (30 Cl⁻ and 120 F⁻) were used, when F⁻ currents were too tiny to measure E_{rev}. For the anion permeability test, individual data were corrected by measuring the

offset potential shift induced by the replacement of anion solution after each experiment.⁷ The 146 mM HCO_3^- -containing solutions were continuously gassed with 95% O_2 and 5% CO_2 and pH adjusted to 8.2, which is comparable to ionic compositions of human pancreatic juice. For the current measurements of ANO1, the free Ca^{2+} concentrations of buffer solutions were achieved by adjusting the Ca^{2+} chelator EGTA (10 mM) and CaCl_2 concentrations using WEBMAX-C software (<http://www.stanford.edu/~cpatton/maxc.html>). Because the Ca^{2+} chelating power of EGTA is weakened in the 1 μM and greater free Ca^{2+} range, the 3 μM free Ca^{2+} -containing solutions were buffered with the low-affinity Ca^{2+} chelator di-bromo-BAPTA (5 mM). The osmolarity of the bath solution was 10 mOsm higher than the pipette solution's osmolarity by adding sorbitol to suppress volume-regulated anion channels.

4. Calculation of Relative Ion Permeability (P_x/P_{Cl}), Dielectric Constant (ϵ), and Pore Size

Current reversal potential (E_{rev}) was measured using zero-current clamp recordings. To evaluate the I-V relationship during the zero-current clamp recordings, current clamp mode was changed to the voltage clamp mode, and I-V curves were obtained by applying ramp pulses from -100 to 100 mV (0.8 mV/ms, holding potential; near the RMP) or step pulses from -100 to 100 mV (voltage interval; 20 mV, duration; 0.5 s, holding potential; near the RMP). The relative anion permeability was calculated from the reversal

potential shift ($\Delta E_{\text{rev}} = E_{\text{rev}}(\text{X}) - E_{\text{rev}}(\text{Cl})$) elicited by replacing extracellular Cl^- with other anion, X^- using the Goldman-Hodgkin-Katz equation : $P_{\text{X}}/P_{\text{Cl}} = (\exp(\Delta E_{\text{rev}}/(RT/zF)) - ([\text{Cl}^-]_{\text{o}}/[\text{Cl}^-]_{\text{o}})) \times ([\text{Cl}^-]_{\text{o}}'/[\text{X}^-]_{\text{o}})$, where $[\text{Cl}^-]_{\text{o}}'$ is the bath concentration of Cl^- , $[\text{Cl}^-]_{\text{o}}$ is the residual Cl^- in the substituted solution, $[\text{X}^-]_{\text{o}}$ is the concentration of substitute ion, and R , T , z , and F have their usual thermodynamic meanings.

The electrostatic model of Born^{4,5} was applied to calculate the dielectric constant (ϵ) of anion channels. Concisely, the hydration energy of each anion can be calculated by the following equation: $\Delta G_{\text{hyd}} = -(K/2) \times (1/r) \times (1 - 1/\epsilon_{\text{w}})$, where K is a constant equal to $138.6 \text{ kJ}\cdot\text{nm}/\text{mol}$, r is the radius of the anion, and ϵ_{w} is the dielectric constant of water ($\epsilon_{\text{w}} = 80$). For optimizing anion-water interaction energy in the dielectric constant calculation, lattimer correction of the equivalent radius of each ion was applied.⁴ $\Delta(\Delta G)_{\text{barrier}}$ for the anions can be calculated from the following equation: $P_{\text{X}}/P_{\text{A}} = \exp[-\Delta(\Delta G)_{\text{barrier}}/RT]$ where A^- was the largest anion examined in the present study (NO_3^- for CFTR, I^- for all other anion channels), and used as the reference anion. Using the $\Delta(\Delta G)_{\text{barrier}}$ of each anion, solvation energy (ΔG_{sol}) of the ion channel can be calculated by the following equation³: $|\Delta G_{\text{sol}}| = |\Delta G_{\text{hyd}}| - |\Delta(\Delta G)_{\text{barrier}}|$. From the ΔG_{sol} value, ϵ of anion channel was calculated by the following equation⁵: $\Delta G_{\text{sol}} = -(K/2) \times (1/r) \times (1 - 1/\epsilon)$.

Pore size of anion channels was estimated by the excluded-area model (partition coefficient model) using the $P_{\text{X}}/P_{\text{Cl}}$ values of large non-symmetrically charged anions.^{9,27,28} According to the excluded-area model,

ionic permeation is proportional to the area of the narrowest region of pore left unoccupied by the ion. P_X/P_{Cl} is then given by the following equation: $P_X/P_{Cl} = ([D_P - D_X]/[D_P - D_{Cl}])^2$, where D_P , D_X , and D_{Cl} are the diameter of the pore, anion X^- , and Cl^- . Because the longest dimension of the ion did not affect its effective permeation, the geometric mean of the two smallest dimensions for each ion was used for D_X .^{4,9}

5. Molecular Dynamics (MD) Simulations of GlyR Structure

1) Preparation of simulation systems: Homology models of human $\alpha 1$ GlyR (GLRA1) WT and P-2' Δ mutant were constructed using MODELLER v9.3 (<https://salilab.org/modeller/>) based on the crystal structure of an open anion-selective GluCl (PDB: 3RIF). The sequence of $\alpha 1$ GlyR was edited to remove the large intracellular loop connecting TM3 and TM4 since the GluCl template does not have this homologous loop. Sequence alignments were generated using Uniprot. For each receptor channel, 100 homology models were built and the model with the lowest "MODELLER objective function" score was selected to further MD relaxations. The MD simulation system was set up using the Visual Molecular Dynamics (VMD) analysis and visualization software. The TM domain of the receptor channel was inserted into the center of a cylinder of pre-equilibrated 1-palmitoyl-2-oleoyl-sn-glycero-3-phosphocholine (POPC) lipid mixture. The outer radii of the cylinder POPC lipid construct was approximately 52.3 Å. Fully equilibrated TIP3 waters were added to the system to form a hexagonal

boundary condition of $104.6 \times 104.6 \times 150$ Å. Na^+ and Cl^- ions corresponding to a 0.15 M solution were added to neutralize the system. There were one receptor channel, 196 POPC, 88 Cl^- ions, 83 Na^+ ions, and about 29,100 water molecules for a total of over 141,000 atoms.

2) Molecular dynamics simulations: The CHARMM force field with CMAP corrections was used for protein, water, and lipid simulations.²⁹⁻³¹ MD simulations were performed using the NAMD2 program.³² Two independent MD runs were performed for the WT GlyR (WT_1 and WT_2) and its P-2'Δ mutant (PΔ_1 and PΔ_2), following the same simulation procedure. The system was first energy minimized for 50,000 steps. It then underwent a 0.5 ns constant volume and temperature ($T = 310$ K) (NVT) simulation and subsequent 4 ns NPT simulation, during which the protein was fixed and the constraint on the POPC head groups was gradually released to zero. Subsequently, the constraint on the protein backbone was gradually reduced from 10 Kcal/mol to zero within 4 ns. Finally, the unconstrained protein underwent NPT simulation for 46 ns. The simulation protocol included periodic boundary conditions, water wrapping, hydrogen atoms constrained via the SHAKE algorithm, and long-range electrostatic forces evaluated via the Particle Mesh Ewald (PME) algorithm.³³ Bonded interactions and short-range nonbonded interactions were calculated every time step (2 fs) and every two time steps (4 fs), respectively. Electrostatic interactions were calculated at every four time-steps. The cutoff distance for nonbonded interactions was 12 Å. A smoothing function was employed for

the van der Waals interactions at a distance of 10 Å. The pair-list of the nonbonded interactions was calculated every 20 time-steps with a pair list distance cutoff of 13.5 Å.

VMD was used to analyze structural and dynamical features of the system, such as the root-mean-square deviation (RMSD), average pore radii, and TM2 helical tilting angles. For structural averaging calculations, each MD snapshot was aligned with the initial model before the determination of an average structure. Radii of the model channels were calculated using the HOLE program.³⁴ The number of water molecules inside the selectivity region was obtained by counting water molecules inside the pore between -2' to 2' ($-50 \text{ Å} \leq z \leq -40 \text{ Å}$). Histogram analysis was performed after the system was well-equilibrated.

3) Halide ion parameterization in the Chemistry at HARvard Macromolecular Mechanics (CHARMM) format: Nonbonded Lennard-Jones (LJ) parameters for Na^+ and Cl^- are directly taken from CHARMM General Force (CGenFF) field.³⁵ LJ parameters for halide ions F^- and I^- are adapted from CGenFF³⁵ and further refined to satisfy experimentally-observed ion solvation properties in water solution, such as radial distribution function (RDF) of ion and oxygen atoms from water (R_O), and number of coordinated water molecules. Calibrations of LJ parameters for halide ions are carried out using MD simulations. For each system, one Na^+ and one halide ion are placed in a 40 Å^3 cubic water box. For each calibration, 6 ns standard Nosé-Hooverconstant pressure^{36,37} ($P = 1 \text{ Bar}$) and temperature ($T = 310 \text{ K}$) (NPT)

simulation is carried out using NAMD2 program.³²

4) Adaptive biasing force (ABF) calculations of the single ion potential mean force (PMF) for ion transport: The single ion PMF for ion transport through the selectivity filter region was carried out using the ABF³⁸ method implemented in the NAMD2 software³² and following the previous approach for similar calculations in other family members of pentameric ligand-gated ion channels (pLGICs).^{39,40} Briefly, ABF calculations of the PMF were carried out in 4~6 different windows along the channel *z* axis (perpendicular to the membrane lipids). The width of each ABF window was 5 Å and five to ten consecutive 1-ns ABF calculations were performed for each window until the variation of the PMF at any point along the *z*-axis was less than 1 kJ/mol within two consecutive runs. The initial configuration for each ABF window was obtained from a 300 ps equilibration simulation that had the target ion positioned within the window. Calculations for different halide ions followed the same procedure and were carried out in the same initial configuration except that only the target ion (transport ion) was replaced by the specific halide ion (I⁻, Cl⁻ or F⁻). The initial configurations for WT GlyR and P-2'Δ mutant were taken from 20-ns MD equilibrated snapshots.

6. Cortical Slice Preparation, Whole-Cell Recording, and GABA Puffing

Whole-cell patch recordings on pyramidal neurons in adult rodent sensorimotor cortical slices were performed as described earlier.⁴¹ All animal

experiments were performed in accordance with the Institutional Guidelines of Animal Care and Use, and utilized protocols were approved by the Korea Institute of Science and Technology. Sensorimotor cortical slices (thickness 400 μm) were obtained from adult C57BL/6 mice (6-8 weeks). Following decapitation, the brain was rapidly removed and placed in cold artificial cerebrospinal fluid (ACSF) having the following composition (in mM): 130 NaCl, 24 NaHCO_3 , 3.5 KCl, 1.25 NaH_2PO_4 , 1 CaCl_2 , 3 MgCl_2 , 10 glucose. Slices were made using an oscillating tissue slicer (DSK PRO7, Kyoto, Japan) at cold ACSF and stored in a bath of oxygenated (95% O_2 and 5% CO_2) ACSF for a recovery period of at least 1 hr. Each slice was transferred from a recovery/holding reservoir to the recording chamber of a fixed-stage upright microscope (BX51WI, Olympus) and submerged in oxygenated ACSF that was supplied to the chamber at a rate of 1.5–2 mL/min.

Whole-cell patch clamp recordings were obtained using borosilicate glass pipettes (resistance 4–10 M Ω) prepared by a 2-stage vertical pipette puller (PC-10, Narishige, Tokyo, Japan). The pipettes were filled with a solution having the following composition (in mM): 100 K-gluconate, 20 KHCO_3 , 20 KCl, 2 NaCl_2 , 20 HEPES, 0.5 EGTA, 10 glucose, 2 Na-ATP, 0.5 Na-GTP; pH was adjusted to 7.3 with KOH. For experiments in HCO_3^- -free, HEPES-buffered solutions, in which equimolar HCO_3^- was replaced with gluconate, slices were preincubated in the HEPES-buffered media for at least 15 min. Voltage-clamp and current-clamp recordings were acquired using a MultiClamp 700A amplifier and pClamp10 software after digitizing signals

by Digidata 1300 series (Molecular Devices). All patch recordings were from layer 2–3 cortical neurons. For the brief application of GABA, the tip of a GABA-containing micropipette was placed within 100–150 μm of the soma. Extracellular GABA was applied with positive air pressure to the GABA-filled micropipette by Picospritzer with 10–30 psi for 10–30 ms.

7. Modeling of $P_{\text{x}}/P_{\text{Cl}}$ using Free Energy of Anions and Pore Diameter of Anion Channels

1) Computation of anion free energy: We employed the polarizable continuum model (PCM) and the density functional theory (DFT) to compute the free energies of anions in a dielectric medium. First, the structures of various anions in the gas phase and in aqueous environment were optimized using DFT at the level of B3LYP/6-311++G(d,p). The integral equation formalism-PCM (IEF-PCM) for solvents was then used to calculate the free energy change of solvation ($\Delta G_{\text{sol}}^{\text{v}}$) and that of hydration ($\Delta G_{\text{hyd}}^{\text{v}}$) of the anions.^{42,43} Due to computational complexity of ions with too many orbitals, Γ^- was excluded from the free energy computation. All calculations presented were carried out using GAUSSIAN03 package (Gaussian, Inc., Wallingford, CT, USA).

2) Modeling of $P_{\text{x}}/P_{\text{Cl}}$: To evaluate the permeability of an anion, thermodynamic and size effects were taken into account as

$$P = P_{\Delta G}^{\alpha} \cdot P_{\text{size}} \quad (1)$$

where P is the relative permeability of an anion ($P_{\text{x}}/P_{\text{Cl}}$), $P_{\Delta G}$ is the P

determined by the free energy of anions, α is a channel-specific weight factor, and P_{size} is the P determined by the pore diameter of anion channels.

The transfer free energy contribution was evaluated as the following

$$P_{\Delta G} = \exp(-\Delta\Delta G_{trans} / RT) \quad (2)$$

where R is the gas constant and T is temperature. The free energy change of transfer is defined as $\Delta\Delta G_{trans} = \Delta G_{solv} - \Delta G_{hyd}$.

To account for the size-dependent effect, we employed a partition coefficient model.⁹ By modeling the ion channel as a hard-wall cylinder, the conventional partition coefficient model often overestimates the permeability for small anions. In addition, recent studies have shown that ion channels are rather flexible.^{44,45} Therefore, in this work we used a shifted partition coefficient model to incorporate the flexibility of ion channel pore upon ion permeation as

$$P_{size} = \left[1 - \frac{\lambda - \lambda_0}{1 - \lambda_0} \right]^2 = \left[1 - \frac{a - a_0}{d - a_0} \right]^2 \quad (3)$$

where $\lambda = a/d$, $\lambda_0 = a_0/d$ with a being the diameter of the ion, d being the diameter of channel pore, and a_0 being the threshold anion diameter.

A channel-specific weight factor α was incorporated into the model as a power to $P_{\Delta G}$ to describe the relative contribution between thermodynamic and size effects. The threshold diameter and channel factor were estimated via the nonlinear least square method using nls function of stats package implemented in R software (ver 3.0.2, freeware).

8. Statistical Analysis

The results of multiple experiments are presented as means \pm SEM. Statistical analysis was performed with Student's *t*-tests or with analysis of variance followed by Tukey's multiple comparison test, as appropriate. $P < 0.05$ was considered statistically significant.

III. RESULTS

1. The $P_{\text{HCO}_3}/P_{\text{Cl}}$ Increases in CFTR and ANO1 have an interaction with electric permittivity and pore size

Previous research showed that Ca^{2+} /calmodulin regulates bicarbonate permeability of ANO1 as well as affects the permeability of other anion, while the ϵ of the hypothetical ANO1 selectivity filter varied.⁶ Therefore, I examined whether a similar phenomenon happens in the CFTR in which $P_{\text{HCO}_3}/P_{\text{Cl}}$ is regulated by WNK1/SPAK pathway. A whole-cell patch recording was performed in HEK 293T cells expressing human CFTR to measure P_X/P_{Cl} of anions with or without activated WNK1/SPAK (Figures 1-6). As reported previously,⁷ the $P_{\text{HCO}_3}/P_{\text{Cl}}$ of CFTR was significantly increased by the WNK1/SPAK activation through low $[\text{Cl}^-]_i$ (Figures 1E and 2E). $P_{\text{HCO}_3}/P_{\text{Cl}}$ did not increase in cells expressing inactivated WNK1/SPAK with a high $[\text{Cl}^-]_i$ (150 mM) (Figure 3). Whereas, the low $[\text{Cl}^-]_i$ (10 mM) in cells expressing CFTR only, which may have endogenous WNK1/SPAK, induced a partial increase in $P_{\text{HCO}_3}/P_{\text{Cl}}$ (Figure 4); however, knockdown of WNK1/SPAK by siRNA treatments abolished this phenomenon (Figure 5). Collectively, the above results reveal that WNK1/SPAK activation is responsible for the low $[\text{Cl}^-]_i$ -induced $P_{\text{HCO}_3}/P_{\text{Cl}}$ increase in CFTR.

Particularly, activated WNK1/SPAK also had influence on the P_X/P_{Cl} of halides and pseudohalide, NO_3^- in addition to HCO_3^- (Figure 2). The P_X/P_{Cl} regulation pattern of CFTR by WNK1/SPAK activation except I^- , resembled that observed in the ANO1 by modulation of Ca^{2+} /calmodulin (see also Figure 6B).⁶ The intervals between the relative permeability (P_X/P_{Cl}) values of large and small ions (e.g. $P_{\text{NO}_3}/P_{\text{Cl}}$ and $P_{\text{F}}/P_{\text{Cl}}$ in Figure 1F and 2F) in CFTR were narrowed by activation of WNK1/SPAK, possibly due to an

increase in the electric permittivity of the CFTR selectivity filter. When the ϵ of the channel pore region increases and becomes close to that of water (ϵ of a vacuum = 1, water = 80), hydration energy differences between the large and small ions decrease. Indeed, ϵ of CFTR pore region increased from 15.5 to 43.3 by WNK1/SPAK activation (estimated from the P_X/P_{Cl} values of NO_3^- , Br^- , and F^- ; Figure 6A).

Although, the P_I/P_{Cl} should be greater than P_{NO_3}/P_{Cl} or P_{Br}/P_{Cl} according to the simple dielectric tunnel theory, the P_I/P_{Cl} of CFTR was lower. Even more, although, theoretically, the P_I/P_{Cl} should decrease when ϵ increases because I^- is bigger than other anions,³⁻⁵ the P_I/P_{Cl} of CFTR showed the opposite. In the control state, the P_I/P_{Cl} of CFTR was 0.41 ± 0.03 (Figure 1D and 1F), and this value means I^- permeability was even smaller than that of the Cl^- ion which is smaller than I^- in CFTR. Furthermore, P_I/P_{Cl} was increased by WNK1/SPAK activation (Figure 2D and 2F), while ϵ of CFTR increased.

Therefore, we thought that the pore size of CFTR is not big enough to pass I^- freely, then the thermodynamic size-exclusion of I^- may limit movement of I^- in the CFTR channel pore. So, I calculated the pore size of CFTR by measuring the permeability of variable large-sized polyatomic anions. The excluded-area model (partition coefficient model) was used for estimation. The pore size of control state CFTR was 4.84 Å (Figure 6A), which is only 10% larger than the diameter of I^- (4.4 Å). Interestingly, the pore size of WNK1/SPAK activated CFTR was increased to 5.34 Å (Figure 6A), which is 21% bigger than the diameter of I^- . This may be a reason why the P_I/P_{Cl} of CFTR was increased after WNK1/SPAK activation.

Because of the small pore size of CFTR, I could obtain measurable

P_X/P_{Cl} values only from the relatively small polyatomic anions (acetate, pyruvate, and propionate). However, the the P_I/P_{Cl} pattern of ANO1 followed theoretical principles, and the high ANO1 P_I/P_{Cl} suggests that ANO1 channel may have a bigger pore size than CFTR.⁶ Therefore, I next conducted the above experiments in ANO1 channel to estimate whether the pore size changes or not. ANO1 is activated by $[Ca^{2+}]_i$ elevation.⁴⁶⁻⁴⁸ It has been shown that ANO1 is poorly permeable to HCO_3^- at a submaximal $[Ca^{2+}]_i$ (400 nM), but at high $[Ca^{2+}]_i$ ($> 1 \mu M$), ANO1 is highly permeable to HCO_3^- which is associated with Ca^{2+} /calmodulin.⁶ The pore size of ANO1 at 400 nM $[Ca^{2+}]_i$ was 7.98 Å (Figure 6B), which is roughly 80% bigger than the diameter of I^- . Hence, the size-exclusion effects were likely negligible and the P_I/P_{Cl} of ANO1 was mainly determined by the permittivity of the pore rather than size-exclusion effects. Importantly, the pore size of ANO1 increased to 8.56 Å at the 3 μM high $[Ca^{2+}]_i$ along with the increase in ϵ reported earlier.⁶ Taken together, the results indicate that the dynamic increase in P_{HCO_3}/P_{Cl} of CFTR and ANO1 was related with increases in electric permittivity and diameter of the channel pore.

CFTR only, 150 mM $[Cl^-]_i$

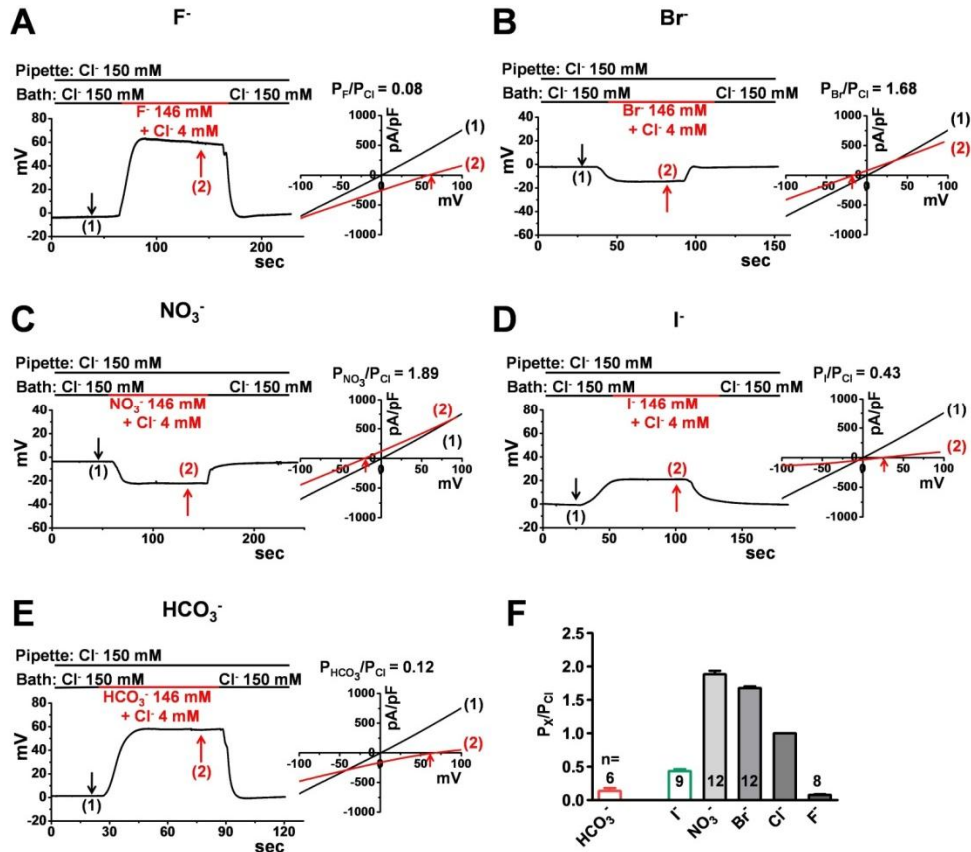


Figure 1. Anion Permeability of CFTR in Control Cells. CFTR was expressed in HEK 293T cells, and whole-cell currents were measured. CFTR currents were activated by cAMP (5 μ M forskolin and 100 μ M IBMX) after whole-cell configuration was established. The initial bath solution containing 150 mM Cl^- was replaced with a solution containing 4 mM Cl^- and 146 mM X^- , with X^- representing the substitute anion. To determine the current-voltage (I-V) relationship during zero-current clamp recordings, clamp mode was shifted to the voltage clamp mode and I-V curve was obtained by applying ramp pulses from -100 to 100 mV (0.8 mV/ms, holding potential; near the resting membrane potential). (A-E) Representative voltage traces, and I-V curves are shown. (F) A summary of the P_X/P_{Cl^-} values from zero-current clamp recordings.

CFTR + WNK1/SPAK, 10 mM $[Cl^-]_i$

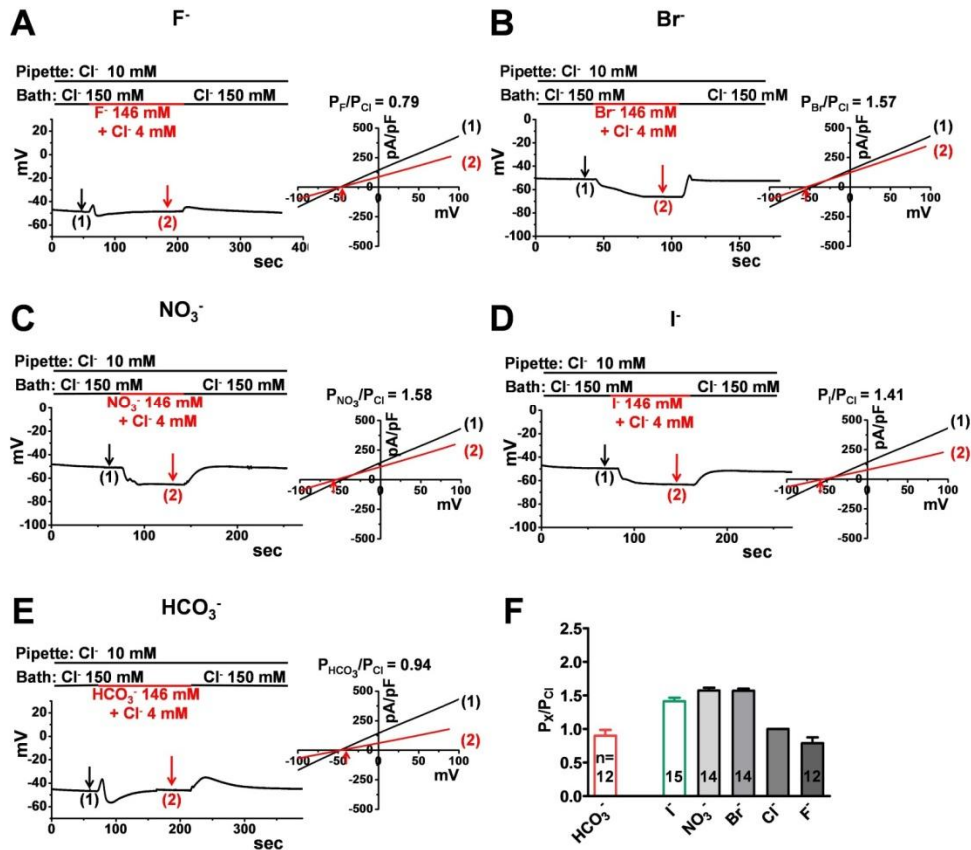


Figure 2. Anion Permeability of CFTR in WNK1/SPAK Activated Cells. CFTR, WNK1, and SPAK were expressed in HEK 293T cells, and whole-cell currents were measured. CFTR currents were activated by cAMP (5 μ M forskolin and 100 μ M IBMX) after whole-cell configuration was established. To activate WNK1/SPAK, low Cl^- (10 mM) pipette solution was used. The initial bath solution containing 150 mM Cl^- was replaced with a solution containing 4 mM Cl^- and 146 mM X^- , with X^- representing the substitute anion. To determine the current-voltage (I-V) relationship during zero-current clamp recordings, clamp mode was shifted to the voltage clamp mode and I-V curve was obtained by applying ramp pulses from -100 to 100 mV (0.8 mV/ms, holding potential; near the resting membrane potential). (A-E) Representative voltage traces, and I-V curves are shown. (F) A summary of the P_X/P_{Cl} values from zero-current clamp recordings.

CFTR + WNK1/SPAK, 150 mM $[Cl^-]_i$

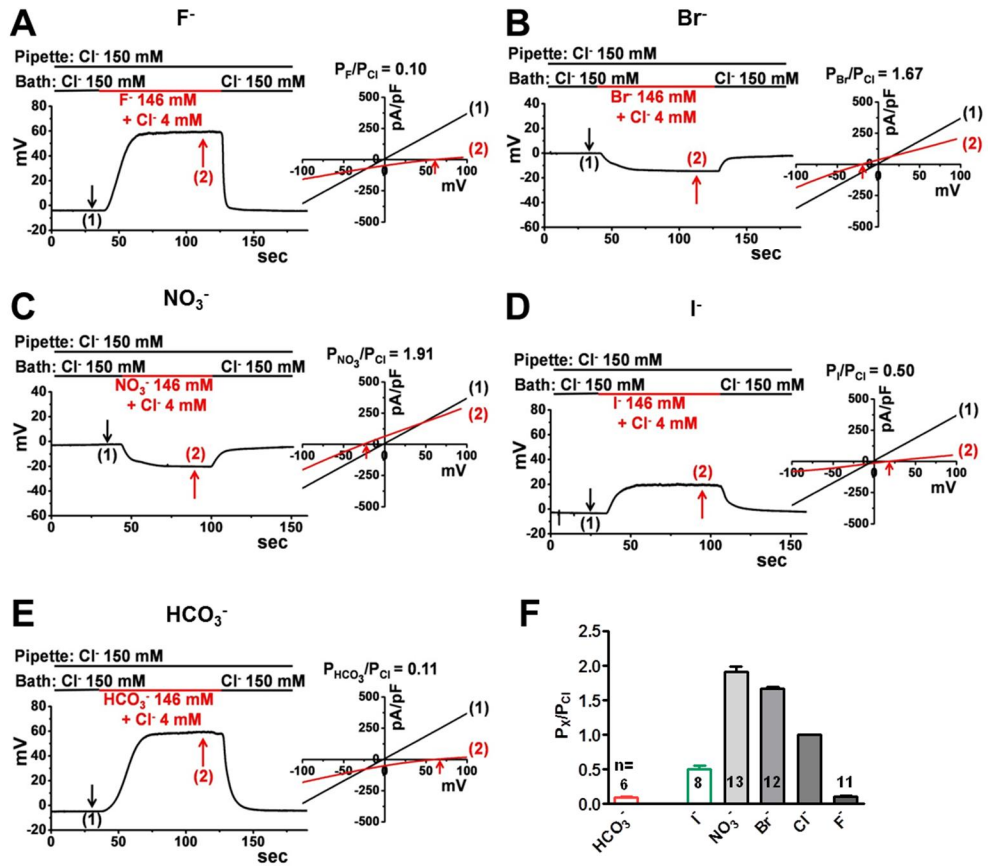


Figure 3. Anion Permeability of CFTR in Cells with Inactivated WNK1/SPAK. CFTR, WNK1, and SPAK were expressed in HEK 293T cells, and whole-cell currents were measured. A high concentration of Cl^- (150 mM) in the pipette did not activate WNK1/SPAK. Same methods were used as Figures 1 and 2. (A-E) Representative voltage traces, and I-V curves are shown. (F) A summary of the P_X/P_{Cl^-} values from zero-current clamp recordings.

CFTR only, 10 mM $[Cl^-]_i$

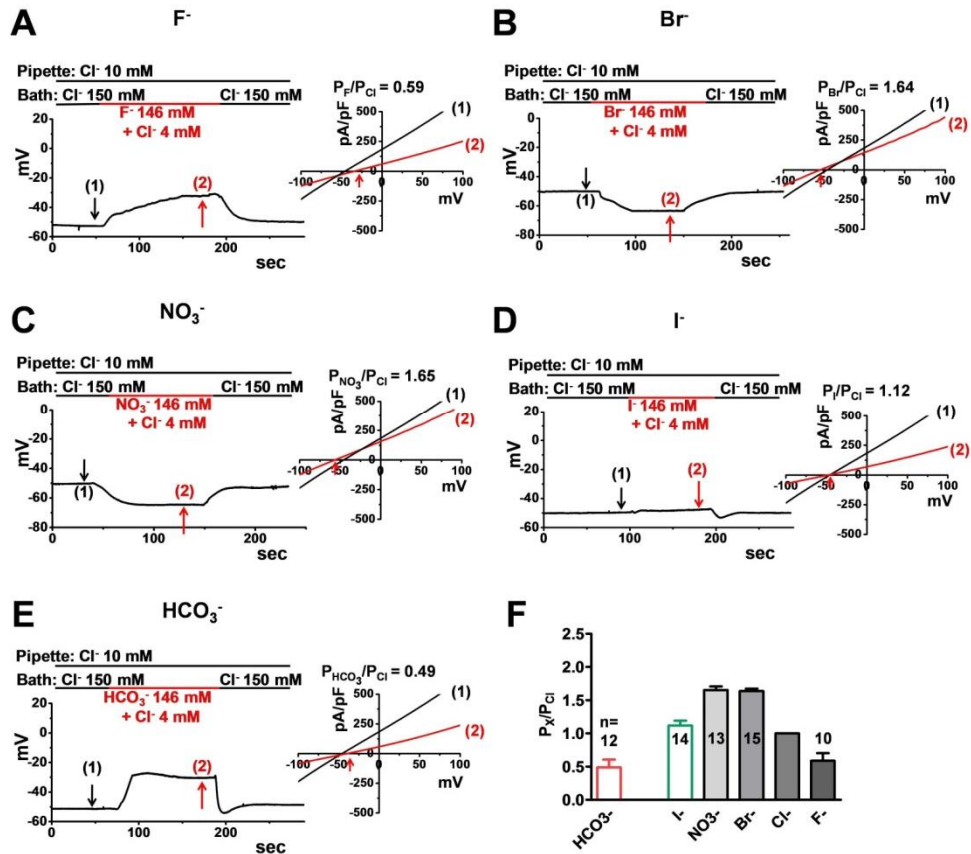


Figure 4. Anion Permeability of CFTR in Control Cells at low $[Cl^-]$. CFTR was expressed in HEK 293T cells, and whole-cell currents were measured. Low (10 mM) Cl^- pipette solution was used. Same methods were used as Figures 1-3. (A-E) Representative voltage traces, and I-V curves are shown. (F) A summary of the P_X/P_{Cl^-} values from zero-current clamp recordings.

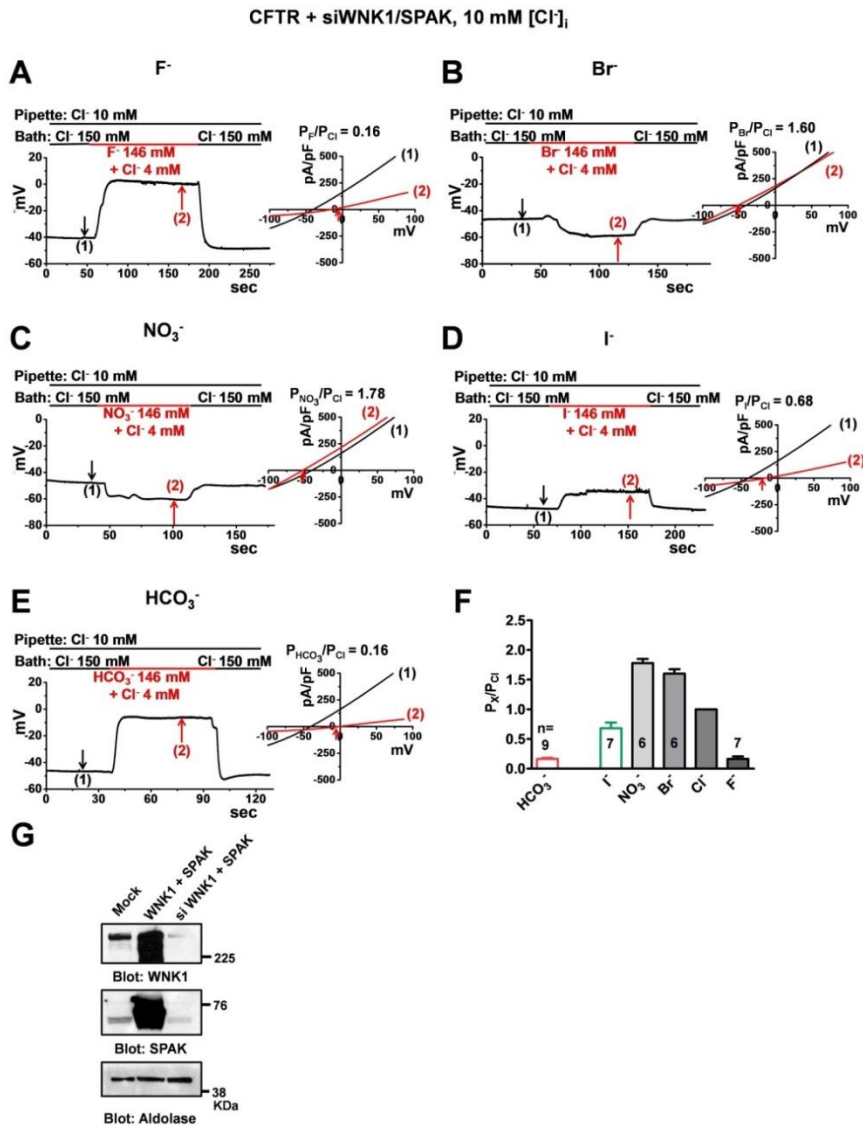


Figure 5. Anion Permeability of CFTR in WNK1/SPAK-Depleted Cells. The plasmids expressing CFTR and siRNAs against WNK1 and SPAK were transfected in HEK 293T cells. Low (10 mM) Cl^- pipette solution was used. Same methods were used as Figures 1-4. (A-E) Representative voltage traces, and I-V curves are shown. (F) A summary of the P_X/P_{Cl^-} values from zero-current clamp recordings. (G) Immunoblotting of WNK1 and SPAK. Treatment with siRNAs against WNK1 and SPAK inhibited endogenous expression of WNK1 and SPAK in HEK 293T cells by $86 \pm 3\%$ and $81 \pm 9\%$ ($n = 3$), respectively.

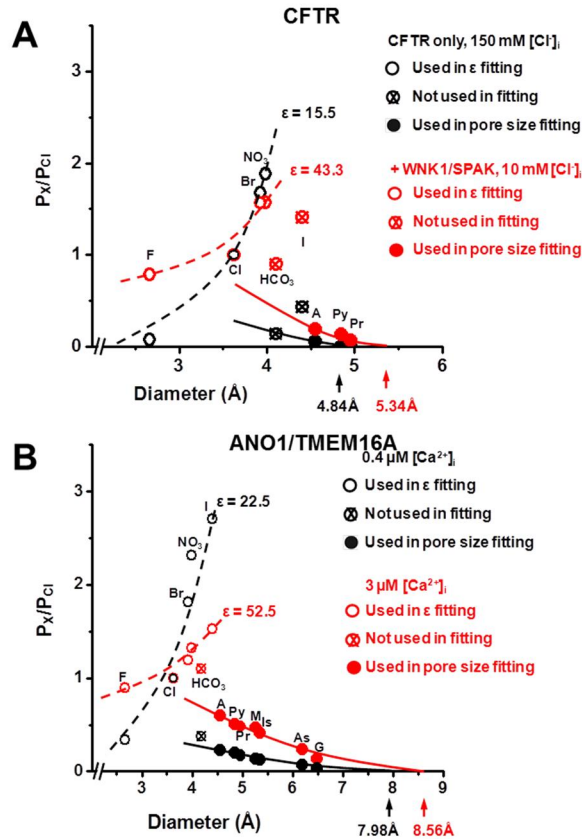


Figure 6. Increased HCO_3^- Permeability is Associated with Increases in Dielectric Constant (ϵ) and Pore Size in CFTR, and ANO1. The plasmids expressing CFTR, and ANO1 were transfected in HEK 293T cells. The x- and y-axes represent the diameter and the relative permeability of each anion, respectively. The dashed lines are the fitted lines for dielectric constant estimation using the electrostatic model of Born and the continuous lines represent the fitted lines for pore size estimation using the excluded-area model. (A) The effects of WNK1/SPAK activation on the CFTR dielectric constant (ϵ) and pore size were analyzed using the P_X/P_{Cl} values of symmetrically charged ions (open circle) and non-symmetrically charged polyatomic ions (filled circle), respectively. (B) The ϵ and pore size of ANO1 were analyzed using submaximal (0.4 μM) or high (3 μM) $[Ca^{2+}]_i$ stimulation. The P_X/P_{Cl} values of halide ions and NO_3^- were from Figures 1 and 2 (A, CFTR), and Jung et al. (2013)⁶ (B, ANO1). A, acetate; As, aspartate; G, gluconate; Is, isethionate; M, methanesulfate; Pr, propionate; Py, pyruvate.

2. Pore Dilation Increases $P_{\text{HCO}_3}/P_{\text{Cl}}$ and ϵ of GlyR by Increasing Water Occupancy in the Selectivity Filter Region

I further researched whether other anion channels have similar phenomena as those described above and if so, how pore dilation leads to an increase in ϵ . I first investigated the GlyR Cl^- channel, which is anion channel located in the spinal cord, brain stem, and several other regions of the central nervous system and functions as synaptic inhibition.⁴⁹ Previous study revealed that pore size of GlyR increases when the proline at the -2 position (P-2' Δ) of the pore-lining second transmembrane segment (TM2) is deleted.¹⁰ Therefore, I examined the P-2' Δ mutant using whole-cell recordings in HEK 293T cells expressing homomeric human α_1 GlyR (GLRA1) (Figure 7). Because P-2' Δ results in increase of Na^+ permeability, and induction of a right shift of the glycine dose-response curve, a higher dose of glycine was applied for the activation of P-2' Δ GlyR, and the Na^+ permeability was corrected for each $P_{\text{X}}/P_{\text{Cl}}$ calculation. The $P_{\text{HCO}_3}/P_{\text{Cl}}$ and ϵ of GlyR were increased in the P-2' Δ mutation in the whole-cell and outside-out patch clamp experiments (Figure 7), which is similar to the responses observed in the CFTR that modulated by WNK1/SPAK activation and Ca^{2+} /calmodulin-induced regulation of ANO1 (Figures 6A and 6B).

The structure of *Caenorhabditis elegans* glutamate-gated channel (GluCl) which is an open-channel and has high homology between hGlyR, was crystalized recently.⁵⁰ The molecular dynamics (MD) simulation was performed to figure out the relationship and influence of pore size on electric permittivity. The modeling of homopentameric GLRA1 indicated that the P-2' Δ mutation increased the GlyR functional diameter of pore from 5.0 to 7.0 Å (radius from 2.5 to 3.5 Å, Figures 8A and 8B) by changing the orientation of the pore lining TM2 helices (Figures 8C-8F). These values were

comparable to those obtained from whole-cell patch clamp recordings (5.3 and 7.1 Å, respectively) (Figure 7E). Particularly, the number of water molecules inside the selectivity filter region increased approximately 25%, by pore enlargement and orientation change of P-2'Δ mutation (Figure 9A). And the energy barriers of halide ion transport were reduced in P-2'Δ mutation (Figures 9B and 9C, Tables 1 and 2). These results indicate that greater water occupancy increased electric permittivity of the GlyR pore. The halide transport data from MD simulations showed that the P-2'Δ increases the estimated ϵ from 15.9 to 34.6 (Figure 9D), and these values were comparable to the values acquired from whole-cell recordings (14.3 and 33.4, respectively) (Figure 9E).

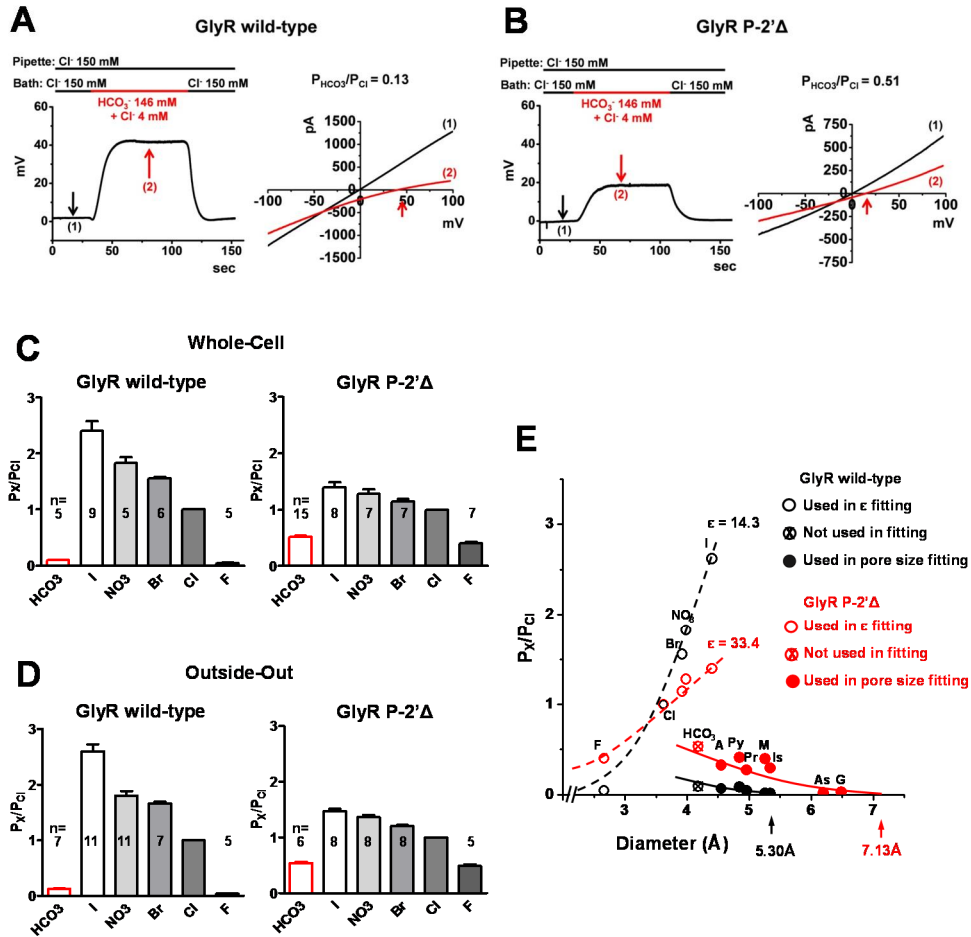


Figure 7. Pore Dilation Increases $P_{HCO_3^-}/P_{Cl^-}$ and ϵ of the Glycine Receptor (GlyR). (A-D) P_X/P_{Cl^-} changes in response to the P-2'Δ mutation-induced GlyR pore dilation were analyzed. Homomeric human α_1 GlyR (hGLRA1) was expressed in HEK 293T cells and whole-cell (A-C) or outside-out (D) patch recordings were performed. Wild-type and P-2'Δ GlyRs were stimulated with 10 μ M and 1 mM glycine, respectively. Examples of $P_{HCO_3^-}/P_{Cl^-}$ measurements are shown in (A and B). Summaries of the P_X/P_{Cl^-} values from the whole-cell and outside-out recordings are shown in (C) and (D), respectively. (E) GlyR dielectric constant (ϵ) and pore size in response to the P-2'Δ mutation were analyzed using the P_X/P_{Cl^-} values of symmetrically charged ions (open circle) and non-symmetrically charged polyatomic ions (filled circle), respectively ($n \geq 5$). Data are means \pm SEM. A, acetate; As, aspartate; G, gluconate; Is, isethionate; M, methanesulfate; Pr, propionate; Py, pyruvate.

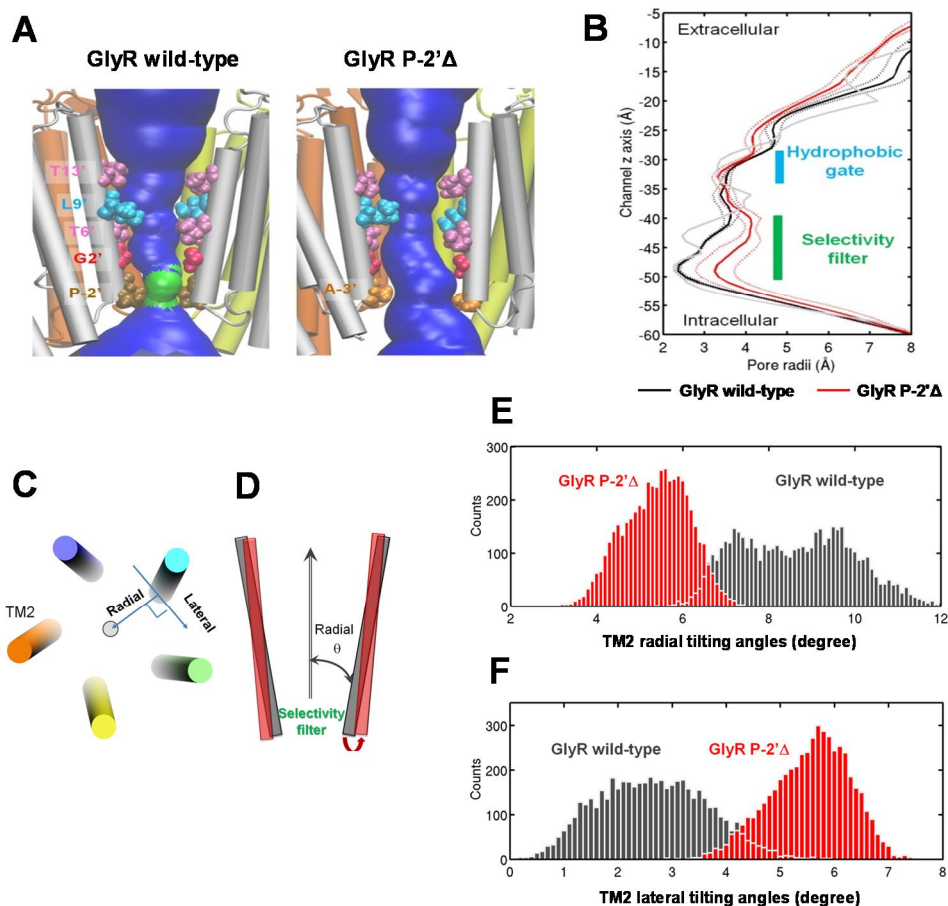


Figure 8. Molecular Dynamic (MD) Analyses of the GlyR Pore. (A) Homopentameric wild-type and P-2'Δ hGLRA1s were investigated using MD simulations and homology modeling based on the homologous open GluCl structure from *Caenorhabditis elegans*. Channel pores inside the TM domains are depicted in green ($2 \text{ \AA} < r \leq 3 \text{ \AA}$, radius) and blue ($r > 3 \text{ \AA}$, radius). The pore-lining residues of TM2 are shown with their position numbers. (B) The P-2'Δ mutation enlarged the GlyR functional pore. The pore radius of wild-type GlyR stabilized at $2.5 \pm 0.2 \text{ \AA}$ (near P-2'). The equilibrated pore radii of P-2'Δ GlyR fluctuated around $3.5 \pm 0.4 \text{ \AA}$ (near A-3'/A-1'). (C-F) GlyR P-2'Δ mutation altered the orientation of the pore lining TM2 helices, contributing to the enlargement of selectivity filter region. (C) Top view of five TM2 helices. Radial and lateral directions for calculating the tilting angles are shown. (D) Side view of the TM2 subunit radial angle in GlyRs. (WT: black cylinder, P-

2' Δ : red transparent cylinder). Perpendicular arrow points to the channel z direction. Decreasing TM2 radial tilting enlarges the selectivity filter in the GlyR P-2' Δ mutant. Histograms of TM2 radial tilting angles (E) and TM2 lateral tilting angles (F) in GlyR wild-type (black) and P-2' Δ mutant (red). A total of 5,000 structures and 0.1° of bin were used in each histogram analysis, which contains independent MD runs from 10 ns to 50 ns.

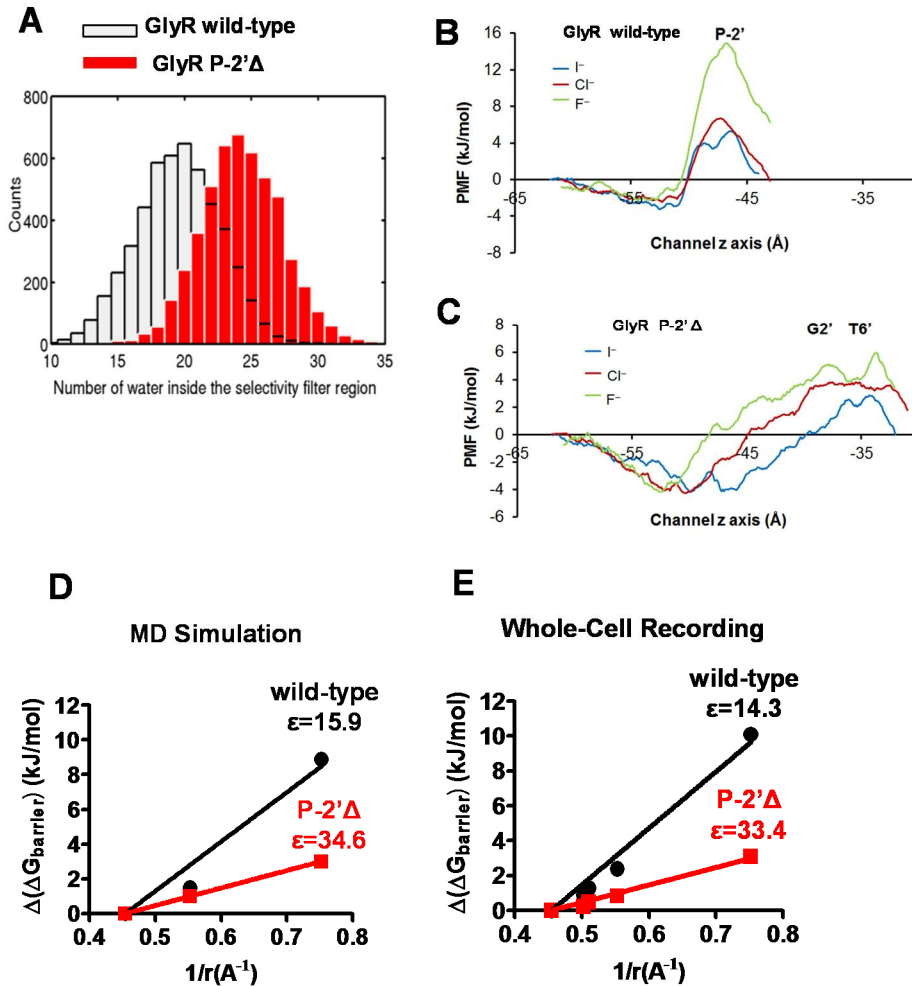


Figure 9. Pore Dilation Increases ϵ of GlyR by Increasing Water Occupancy in the Selectivity Filter Region. (A) Histograms depicting water inside the selectivity filter region of the equilibrated GlyR wild-type (gray) and P-2'Δ mutant (red). A total of 5,000 structures and 40 bins were used in each histogram analysis, which contains independent runs from 10 ns to 20 ns. The water content inside the selectivity filter region is increased by 25% due to the P-2'Δ mutation. (B and C) Adaptive biasing force (ABF) calculations of the single ion potential of mean force (PMF) for ion transport through the selectivity filter region. Comparisons of the single ion PMF for transporting an I⁻ (blue), Cl⁻ (red), or F⁻ (green) ion through the selectivity filter region of GlyR WT (B) and P-2'Δ mutant (C) are shown. For each halide ion (I⁻, Cl⁻ or F⁻), ABF calculations of the PMF started from the intracellular

entrance and were carried out in four (WT) and six (P-2'Δ) windows along the ion transport direction (the channel z axis). Each window had a width of 5 Å, and five to ten consecutive 1-ns ABF calculations were performed for each window. Over 100 ns and 140 ns of ABF calculations were performed for WT and P-2'Δ GlyRs, respectively. (D and E) The P-2'Δ mutation increased ϵ in the selectivity filter. Data sets of $\Delta(\Delta G_{\text{barrier}})$ between different halide ions and NO_3^- calculated by MD simulation (D) and Figure 7C (E, Whole-Cell Recording) were used to calculate ϵ , using the biggest ion I^- as a reference.

Table 1. Lennard-Jones (LJ) and Electrostatic Parameters Used in the Simulations

Ions	Charge (e)	ϵ_1 (kcal/mol)	$R_{\min}/2$ (Å)	R_o (Å)	
				MD	Exp ^a
Na ⁺	+1	-0.047	1.36	2.35	2.3~2.4
Cl ⁻	-1	-0.150	2.27	3.15	3.1~3.2
F ⁻	-1	-0.135	1.85	2.65	2.6~2.7
I ⁻	-1	-0.215	2.65	3.55	3.5~3.6

ϵ_1 and R_{\min} are depth of the LJ potential well and lowest energy interaction distance, respectively. R_o is the distance between the ion (column 1) and the closest oxygen atom on the first hydration shell. ^aMagini, M. In *Ions and Molecules in Solution*; Tanaka, N., Ohtaki, H., Tamamushi, R., Eds.; Elsevier: Amsterdam 1983 p97.

Table 2. Comparison of Energy Barriers for Ion Transport across the Selectivity Filter Region Deduced from MD Calculations

	GlyR WT		GlyR P-2'Δ mutant	
	$\Delta G_{\text{barrier}}$	$\Delta(\Delta G_{\text{barrier}})^{\text{a}}$	$\Delta G_{\text{barrier}}$	$\Delta(\Delta G_{\text{barrier}})^{\text{a}}$
	(kJ/mol)	(kJ/mol)	(kJ/mol)	(kJ/mol)
F⁻	14.2 ± 2.5	8.9 ± 2.5	5.8 ± 1.5	3.0 ± 1.5
Cl⁻	6.8 ± 1.0	1.5 ± 1.0	3.8 ± 1.5	1.0 ± 1.5
I⁻	5.3 ± 1.0	0	2.8 ± 1.5	0
Na⁺	21.2 ± 4.0		12.8 ± 2.0	

^a I⁻ was used as the reference anion.

3. Increased HCO_3^- Efflux from GABA_AR Evokes Neuronal Excitation

Next, I examined ion permeation through GABA_AR , which plays a central role in inhibitory neurotransmission in the brain.²⁵ The $\alpha 1$, $\beta 3$, and $\gamma 2\text{L}$ subunits of h GABA_AR were expressed in HEK 293T cells, and whole-cell recordings were performed. $P_{\text{HCO}_3^-}/P_{\text{Cl}^-}$ of h GABA_AR was approximately 0.2 in response to 3 μM GABA. Notably, a high concentration of GABA stimulation (1 mM) led to a biphasic increase (a peak followed by a small sustained elevation) in $P_{\text{HCO}_3^-}/P_{\text{Cl}^-}$ (Figures 10A and 10B). Similar to the other channels I studied, the $P_{\text{HCO}_3^-}/P_{\text{Cl}^-}$ increase in the GABA_AR was associated with increased ε (Figures 10C-10G). Because of an extremely small permeability to F^- , the increase in ε was more evident when the permeability value of F^- was excluded (Figure 10G, inset).

As introduced earlier, an intensive GABA_AR stimulation paradoxically produces neuronal excitation. An increase in $[\text{Cl}^-]_i$ due to Cl^- influx through the activated GABA_AR is thought to be responsible for the GABA_AR -mediated excitation.^{24,41} To mimic this state, I performed whole-cell recordings on pyramidal neurons in adult rodent sensorimotor cortical slices with moderately elevated $[\text{Cl}^-]_i$ (22 mM) and strong GABA stimulation (10 mM) (Figure 11). The 10 mM GABA puff evoked an average depolarization of 21.1 mV in the HCO_3^- -containing solutions and 12.4 mV in the HEPES-buffered solutions (5.5 mV in the solutions equilibrated with 100% O_2) (Figure 11E), suggesting that the $P_{\text{HCO}_3^-}/P_{\text{Cl}^-}$ of GABA_AR reached 0.7 at this state (see Discussion). Surprisingly, the 21.1 mV depolarization in the HCO_3^- -containing solutions evoked action potentials in five of the seven experiments (Figure 11B). Conversely, action potentials were not observed in any of the ten experiments with HEPES-buffered solutions (Figure 11B),

indicating that the HCO_3^- efflux is critical to the GABA_AR -mediated excitation in pyramidal neurons.

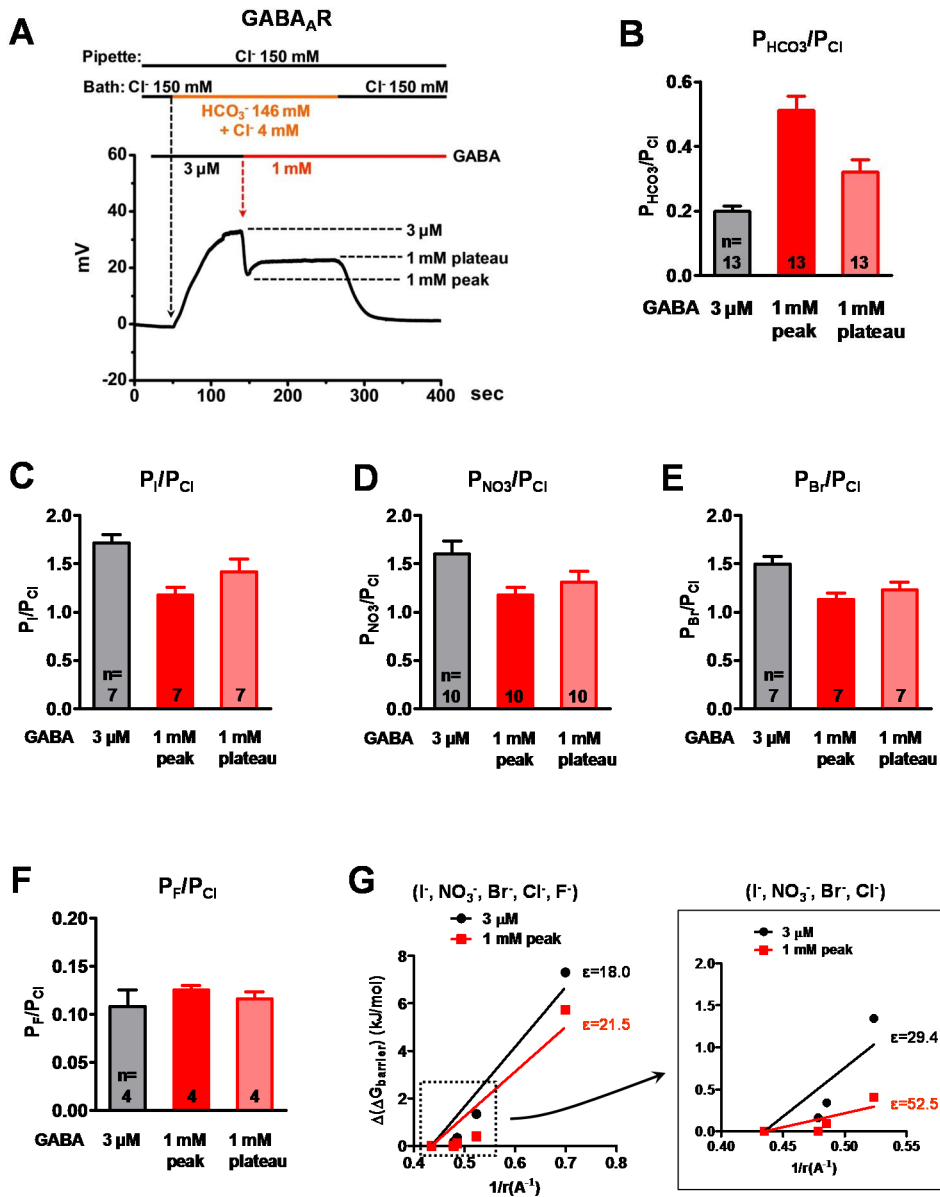


Figure 10. High-Dose GABA Stimulation Increases $P_{\text{HCO}_3}/P_{\text{Cl}}$ and ϵ of GABA_AR. The $\alpha 1$, $\beta 3$, and $\gamma 2\text{L}$ subunits of hGABA_AR were expressed in HEK 293T cells, and whole-cell recordings were performed. (A and B) High-dose GABA (1 mM) stimulation induced a biphasic increase (a peak followed by a plateau) in $P_{\text{HCO}_3}/P_{\text{Cl}}$. An example of $P_{\text{HCO}_3}/P_{\text{Cl}}$ measurement is shown in (A), and summaries of multiple experiments are shown in (B). (C-

F) High-dose GABA (1 mM) stimulation induced a biphasic decrease (a peak followed by a plateau) in P_I/P_{Cl} (C), P_{NO_3}/P_{Cl} (D), and P_{Br}/P_{Cl} (E). P_F/P_{Cl} was not altered by the 1 mM GABA stimulation (F). Summaries of multiple experiments are depicted. (G) High-dose GABA (1 mM) stimulation increased ϵ . The increase in ϵ was more evident when F^- was excluded from the analysis (inset).

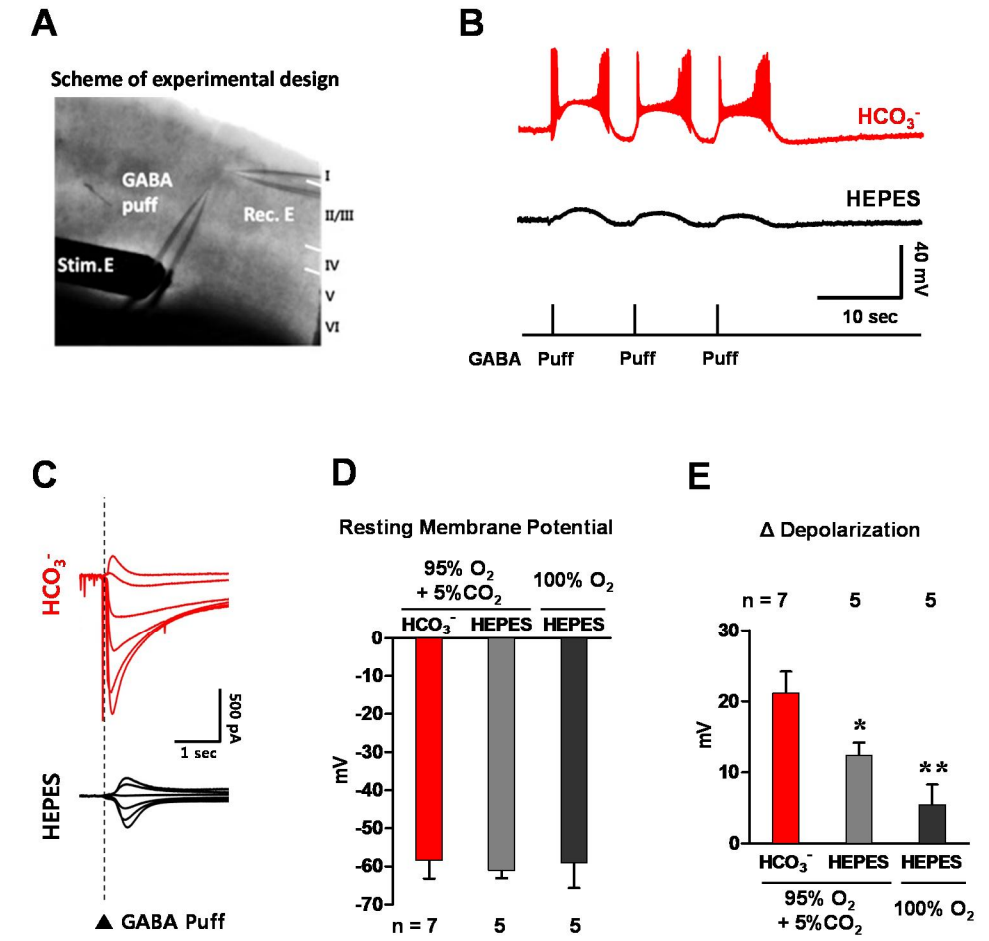


Figure 11. Increased HCO_3^- Efflux through GABA_A Receptors Evokes Neuronal Excitation. (A) Setup for whole-cell patch recordings of pyramidal neurons. Sensorimotor cortical slices (thickness 400 μm) were obtained from adult C57BL/6 mice (6-8 weeks old). All patch recordings were from layer 2–3 (II/III) cortical neurons. The tip of a GABA-containing micropipette was placed within 100–150 μm of the soma, and extracellular GABA (10 mM) was briefly applied using a Picospritzer with positive air pressure (10-30 psi) to the GABA-filled micropipette for 10–30 ms. (B and C) Whole-cell recordings were performed on pyramidal neurons in adult rodent sensorimotor cortical slices. Representative examples of the membrane potential measurements (B) and current-voltage relationship analyses (C) are presented. Note that GABA puffs in the HCO_3^- -containing solutions evoked action potentials (B). (D and E) Summary of the membrane potential measurements. In some

experiments, the HEPES-buffered solutions were equilibrated with 100% O₂ to create absolutely HCO₃⁻-free conditions. A high-dose GABA (10 mM) puff evoked an average depolarization of 21.1 ± 3.0 mV in the HCO₃⁻-containing solutions and 12.4 ± 1.8 mV in the HEPES-buffered solutions (5.5 ± 2.8 mV in the solutions equilibrated with 100% O₂) (D). * $P < 0.05$, ** $P < 0.01$: difference from the first lane.

4. A model to predict Ion Selectivity of Anion Channels using Electric Permittivity and Pore size

To give an overview of a generalized principle of ion permeation via anion channels, I computed the thermodynamic hydration energy effect of each ion in a dielectric medium (Figure 12A) and estimated the P_X/P_{Cl} values by multiplying the pore size effects calculated by the shifted partition coefficient model (Figure 12B, Table 3). The computed values fit well with the P_X/P_{Cl} values measured by the patch clamp experiments of GlyR, ANO1, and CFTR (Figure 12C-12E). In these figures, anions are categorized into two groups. The permeability of symmetrically charged anions, such as halides and NO_3^- , is mainly regulated by electric permittivity, whereas the permeability of non-symmetrically charged polyatomic anions is principally governed by the pore size because non-symmetrically charged polyatomic anions have large dehydration energy barrier in the dielectric medium of anion channel.

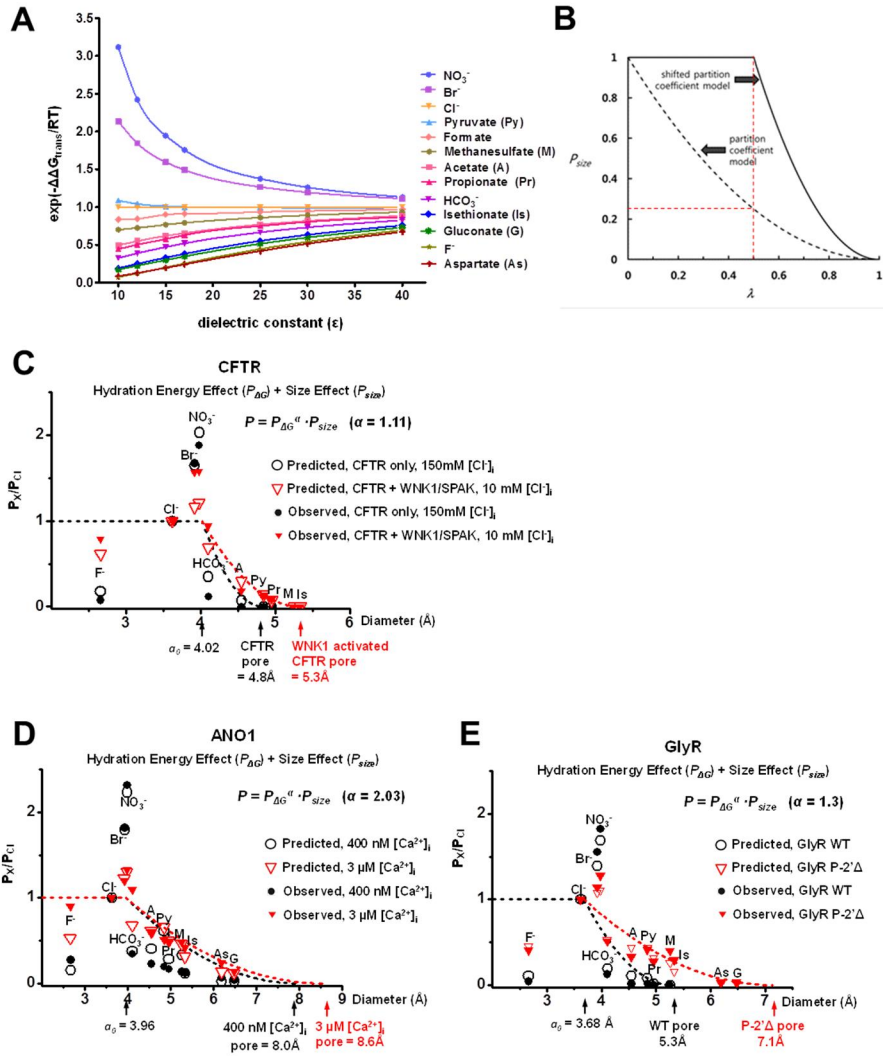


Figure 12. The Pore Size and Thermodynamic Energy Contribute to the Ion Selectivity of Anion Channels. (A) Relationship between the solvent dielectric constant and the hydration energy effect on P_X/P_{Cl} (P_{DG}). Free energies of transfer ($\Delta G_{trans} = \Delta G_{solvation} - \Delta G_{hydration}$) in a dielectric medium were computed using the polarizable continuum model and the density functional theory. In each ion, the relative free energy of transfer with respect to Cl⁻ was calculated ($\Delta\Delta G_{trans} = \Delta G_{trans}[\text{ion X}] - \Delta G_{trans}[\text{Cl}^-]$), and the value was converted to the relative ion permeability ($P_{DG} = \exp(-\Delta\Delta G_{trans}/RT)$). (B) Comparison of the (conventional) partition coefficient model and a shifted partition coefficient model at the threshold diameter $a_0 = 0.5d$. Because the conventional partition coefficient (excluded area)

model overestimates inverse size dependency of P_{size} particularly for tiny ions, threshold diameter (a_0) was employed to limit the maximum size-exclusion effect. The x-axis represents the ratio between the diameters of the ion and channel pore ($\lambda = a/d$) and the y-axis represents the pore size effect on P_X/P_{Cl} (P_{size}). P_{size} of ions with a diameter smaller than a_0 is progressively increased in the conventional partition coefficient model (up to 4-fold at $a_0 = 0.5d$), whereas P_{size} remains constant in the shifted partition coefficient model. (C–E) The P_X/P_{Cl} values of GlyR (C), ANO1 (D) and CFTR (E) were estimated by multiplying the hydration energy effect ($P_{\Delta G}$) by the pore size effect (P_{size}). P_{size} was calculated by the shifted partition coefficient model. The channel-specific factor (α) and a_0 were determined by fitting the experimental values. The predicted values were fitted well with experimental values. Dashed line represents P_{size} ($\alpha = 0$).

Table 3. Dielectric Constant (ϵ), Channel Pore Diameter (d), Threshold Ion Diameter (a_0), and Channel-Specific Weight Factor (α)

Channel	ϵ	d (Å)	a_0 (Å)	α
CFTR only, 150 mM $[\text{Cl}^-]_i$	15.5	4.84	4.02	1.11
CFTR+WNK1+SPAK, 10 mM $[\text{Cl}^-]_i$	43.3	5.34		
ANO1, 0.4 μM $[\text{Ca}^{2+}]_i$	22.5	7.98	3.96	2.03
ANO1, 3 μM $[\text{Ca}^{2+}]_i$	52.5	8.56		
GlyR WT	14.3	5.30	3.68	1.30
GlyR P-2' Δ	33.4	7.13		

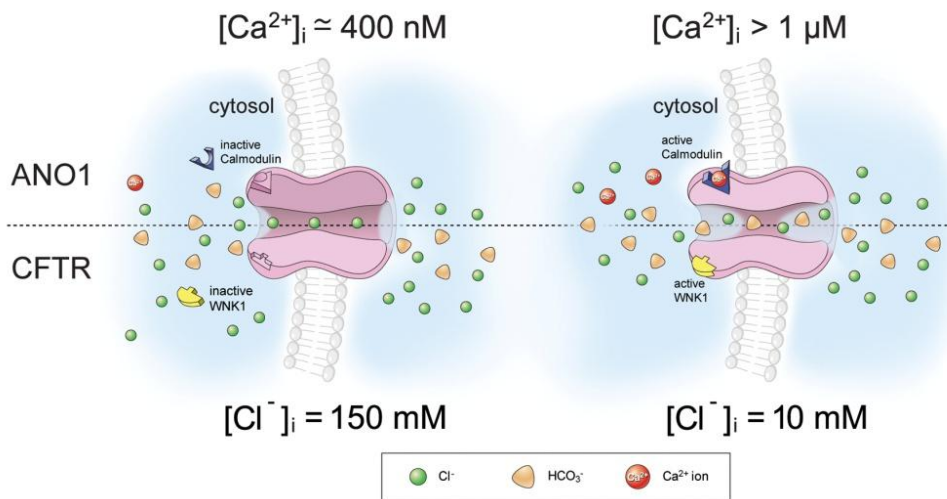


Figure 13. An Illustrated Model for the Dynamic Increase of P_{HCO_3}/P_{Cl} in Anion Channels. Activated WNK1/SPAK and Ca^{2+} /calmodulin enlarged the pores of CFTR and ANO1, respectively. Pore dilation increased the water occupancy and electric field strength in the selectivity filter region.

IV. DISCUSSION

Through combined molecular, physiological, structural, and mathematical approaches, we provide evidence that change in pore size dynamically modulates ion selectivity of anion channels by influencing energy barriers of size-exclusion and ion dehydration. Although pore size change may influence the permeability of many anions, increase in permeability of HCO_3^- through the enlarged pore is markedly prominent (Figure 13). Electrophysiological data obtained from four different anion channels demonstrated a common finding that an increase in $P_{\text{HCO}_3}/P_{\text{Cl}}$ is related with increases in ϵ and the channel pore diameter. When ϵ is below or around 20, $P_{\text{HCO}_3}/P_{\text{Cl}}$ mainly follows the excluded area model. However, as $P_{\text{HCO}_3}/P_{\text{Cl}}$ increases substantially, the pore size and ϵ increase, because of the reduction in the size-exclusion barrier and the decrease in the solvation energy variation between Cl^- and HCO_3^- in an increased dielectric constant medium.

Dynamic increase of $P_{\text{HCO}_3}/P_{\text{Cl}}$ in anion channels is associated with various areas of human physiology and pathophysiology. For example, we have recently demonstrated that several identified CFTR mutations in the chronic pancreatitis, chronic rhinosinusitis, and male infertility, are associated with aberrant HCO_3^- secretion in humans.¹³ Furthermore, reduced CFTR-dependent HCO_3^- secretion in pigs with cystic fibrosis causes abnormalities in the pH of the airway surface liquid and reduces its ability to eradicate bacterial pathogens.⁵¹ Interestingly, many epithelia in which CFTR mediates HCO_3^- secretion, express ANO1 in the apical membrane. Therefore, investigation of the $P_{\text{HCO}_3}/P_{\text{Cl}}$ -modulating mechanism in ANO1 and facilitation of ANO1-mediated HCO_3^- secretion may provide a

pharmacologically appropriate target for disease treatment caused by impaired CFTR.

GABAergic transmission is assumed to provide the main excitatory drive in neuronal networks, at a time when glutaminergic synaptic contacts are less frequent than GABAergic synapses.^{25,52} In addition, neuronal depolarization induced by a massive activation of GABA_AR contributes to epileptogenesis.²⁵ According to a previous study, accumulation of Cl⁻ inside the neuron and collapse of the electrochemical gradient for Cl⁻ are responsible for GABA_AR-induced depolarization.²⁴ In fact, we recently showed that a strong GABA_AR-stimulation evoked an average of 9.9 mM [Cl⁻]_i elevations in pyramidal neurons.⁴¹ However, present results suggest that the [Cl⁻]_i elevation alone is not sufficient to evoke neuronal excitation. Results in Figure 11 clearly indicate that HCO₃⁻ efflux is required for generation of the GABA puff-induced action potentials in pyramidal neurons even at > 20 mM [Cl⁻]_i.

As shown in Figure 10, increasing GABA concentrations from 3 μM to 1 mM increased the GABA_AR P_{HCO3}/P_{Cl} from 0.2 to 0.5. P_{HCO3}/P_{Cl} of mammalian GABA_AR is approximately 0.2 in most experiments involving GABA stimulation with micromolar concentrations.^{25,52} However, at P_{HCO3}/P_{Cl} of 0.2, contribution of the HCO₃⁻ efflux to E_{GABA} will be quite low and the efflux of HCO₃⁻ through the GABA_AR ionophore will induce only a 3.4 mV additional depolarization in experiments with pyramidal neurons (Figure 11) according to the Goldman-Hodgkin-Katz (GHK) equation. In Figure 11, GABA puffs (10 mM) evoked a 12.4 mV depolarization in the HEPES-buffered solutions (resting membrane potential = -61.1 mV) due to Cl⁻ efflux, showing that E_{GABA} (-48.7 mV) was close to E_{Cl} (-47.5 mV). Notably, the same 10 mM GABA puff induced a 21.1 mV depolarization in

the HCO_3^- -containing solutions (resting membrane potential = -58.4 mV), and the additional 8.7 mV depolarization mediated by the HCO_3^- efflux was critical for generation of action potentials (Figure 11B). The E_{GABA} value in the HCO_3^- -containing solutions (-37.3 mV) and membrane depolarization difference between HEPES-buffered and HCO_3^- -containing solutions (8.7 mV) highly suggest that the $P_{\text{HCO}_3^-}/P_{\text{Cl}^-}$ of $\text{GABA}_{\text{A}}\text{R}$ reached 0.7 in this state.

Previously, ion selectivity of a certain channel is believed to be an invariant value. However, several studies revealed that ion selectivity is dynamically regulated by cellular stimuli or agonist concentration. CFTR and ANO1 are previously discussed,^{6,7} furthermore ion selectivity of the transient receptor potential vanilloid 1 (TRPV1) cation channel is also changed by prolonged exposure to capsaicin, which induced increase in the $P_{\text{Ca}}/P_{\text{Na}}$ of TRPV1 by a $[\text{Ca}^{2+}]_{\text{o}}$ -dependent manner.⁵³ Interestingly, the pore dilation was occurred, when capsaicin-induced change in TRPV1 $P_{\text{Ca}}/P_{\text{Na}}$ happened.⁵³ However, the underlying mechanism was not elucidated in the study. Furthermore, pore dilation of chicken BEST1, a Ca^{2+} -activated Cl^- channel, was recently observed by X-ray crystallography, when Ca^{2+} is bound to the Ca^{2+} clasp of the channel and activates the channel.⁵⁴ These findings are similar to results obtained in the present study that strong agonist stimulations increase the pore diameter of ANO1 and $\text{GABA}_{\text{A}}\text{R}$. With these results, it can be suggested that pore dilation of an ion channel take place not uncommonly.

Structural analyses of the GlyR WT and pore-dilated mutant (P-2' Δ) demonstrated that pore dilation increases the electric permittivity of selectivity filter by increasing water occupancy in the pore region. Three conclusions can be inferred from these MD simulations. First, the deletion of proline at -2' position altered the shape of channel pore region and relocated

the position of the selective filter barrier. The proline residue at the -2' position in wild type GlyR cramped pore size of the channel and determined charge selectivity. However, in the P-2' Δ mutant, the peak of the free energy barrier occurred at the threonine residue at the 6' position, indicating the shift of selectivity filter by mutation (Figures 9B and 9C). Second, the relative permeability ratio among halide ions was decided by the minimum channel pore size. This is generally true if no charged residues line the selectivity filter region, as was the case in the WT GlyR and its P-2' Δ mutant, and the energy barrier for ion transport is mainly due to the ion dehydration penalty. In the WT GlyR (minimum pore radius $\sim 2.5 \pm 0.2$ Å), partial dehydration was showed for all permeant ions. Our MD calculations demonstrated that when the minimum pore radius of the channel was larger than 4 Å (diameter 8 Å), the variation in permeability among halide ions was nearly eliminated. Third, ϵ is increased along the enlargement of minimum channel pore size because of increased occupying water molecules in the pore (Figure 9A). Consequently, the calculations using dielectric constant generally agreed with the change in the free energy barrier [$\Delta(\Delta G_{\text{barrier}})$] among different halide ions (Figures 9D and 9E).

The present study was the first to quantify ion selectivity of a given anion channel using hydration energy and pore-size effects. Recent crystallographic analyses of the CLC, GluCl, and BEST1 channels indicate that weak positive helical dipoles, rather than fixed positive charges in amino acids, constitute the selectivity filter of anion channels.^{50,54,55} These findings agree with the previous assumption that weak field strength sites within the channel determine the selectivity of anion channels.⁵⁶ Therefore, hydration forces dominate the ion selectivity sequence because ions must be at least partially dehydrated to pass through the narrow channel filter region. With

symmetrically charged anions such as halides and NO_3^- , hydration energy is inversely correlated with the ionic diameter and thus P_x/P_{Cl} directly related to the ionic diameter. However, when the ionic diameter is larger than critical length, P_x/P_{Cl} decreases due to limitations in the finite channel pore size, as we have shown with the CFTR $P_{\text{I}}/P_{\text{Cl}}$ (Figures 1 and 2). Interestingly, P_x/P_{Cl} was highest for anions with a diameter of about 4 Å in GlyR and GABA_AR of mammalian hippocampal neurons,² and this value is compatible with the threshold ion diameters (a_0) obtained in the present study.

The ion selectivity determination rules described here can be applied to most anion channels which have a moderately sized pore. However, a channel has specific differences. For example, the small F^- permeability of GABA_AR (Figure 10F) may be associated with a specific binding between the channel protein and F^- , as has been shown in CLC-ec1.⁵⁷ In addition, the observed $P_{\text{HCO}_3^-}/P_{\text{Cl}}$ values of ANO1 were a little higher than the values predicted by the modeling, even more than 1. It can be assumed that the channel pore dilation in a single dimension creates an elliptical enlargement in the cross-sectional area of the pore, which helps the permeation of HCO_3^- more, because of planar triangular shape of HCO_3^- and spherical shape of Cl^- . Future studies will be performed to elucidate the meanings and mechanisms explaining channel-specific factors using high-resolution channel structures.

I provide evidence that ion selectivity of anion channels are determined by electric permittivity and pore size, and pore dilation increases ϵ by increasing water occupancy in the pore region. These findings help to elucidate the mechanisms concerning the determination of ion permeation and selectivity, and give us potential therapeutic targets to deal with human diseases associated with aberrant anion permeation. Specifically, agents that

target HCO_3^- permeation in CFTR and ANO1 may be an attractive option for the treatment of epithelial disorders such as cystic fibrosis, and those that target HCO_3^- permeation in GlyR and GABA_AR may help treat neuronal diseases such as epilepsy.

V. CONCLUSION

1. Ion selectivity of anion channel is determined by electric permittivity and pore size.
2. Cellular stimuli can modulate anion channel ion selectivity by changing pore size.
3. Pore size change affects the energy barriers of size-exclusion and ion dehydration.
4. Dynamic change in $P_{\text{HCO}_3}/P_{\text{Cl}}$ may regulate many physiological and pathological processes.

REFERENCES

1. Gouaux E, Mackinnon R. Principles of selective ion transport in channels and pumps. *Science* 2005;310:1461-5.
2. Fatima-Shad K, Barry PH. Anion permeation in GABA- and glycine-gated channels of mammalian cultured hippocampal neurons. *Proc Biol Sci* 1993;253:69-75.
3. Qu Z, Hartzell HC. Anion permeation in Ca^{2+} -activated Cl^- channels. *J Gen Physiol* 2000;116:825-44.
4. Smith SS, Steinle ED, Meyerhoff ME, Dawson DC. Cystic fibrosis transmembrane conductance regulator. Physical basis for lyotropic anion selectivity patterns. *J Gen Physiol* 1999;114:799-818.
5. Born M. Volumen und hydrationwärme der ionen. *Z. Phys* 1920;1:45-8.
6. Jung J, Nam JH, Park HW, Oh U, Yoon JH, Lee MG. Dynamic modulation of ANO1/TMEM16A HCO_3^- permeability by Ca^{2+} /calmodulin. *Proc Natl Acad Sci U S A* 2013;110:360-5.
7. Park HW, Nam JH, Kim JY, Namkung W, Yoon JS, Lee JS, et al. Dynamic regulation of CFTR bicarbonate permeability by $[\text{Cl}^-]_i$ and its role in pancreatic bicarbonate secretion. *Gastroenterology* 2010;139:620-31.
8. Sheppard DN, Rich DP, Ostedgaard LS, Gregory RJ, Smith AE, Welsh MJ. Mutations in CFTR associated with mild-disease-form Cl^- channels with altered pore properties. *Nature* 1993;362:160-4.
9. Linsdell P, Tabcharani JA, Rommens JM, Hou YX, Chang XB, Tsui LC, et al. Permeability of wild-type and mutant cystic fibrosis transmembrane conductance regulator chloride channels to polyatomic anions. *J Gen Physiol* 1997;110:355-64.
10. Lee DJ, Keramidas A, Moorhouse AJ, Schofield PR, Barry PH. The contribution of proline 250 (P-2') to pore diameter and ion selectivity in the human glycine receptor channel. *Neurosci Lett* 2003;351:196-200.

11. Virginio C, MacKenzie A, Rassendren FA, North RA, Surprenant A. Pore dilation of neuronal P2X receptor channels. *Nat Neurosci* 1999;2:315-21.
12. Kaila K, Pasternack M, Saarikoski J, Voipio J. Influence of GABA-gated bicarbonate conductance on potential, current and intracellular chloride in crayfish muscle fibres. *J Physiol* 1989;416:161-81.
13. LaRusch J, Jung J, General IJ, Lewis MD, Park HW, Brand RE, et al. Mechanisms of CFTR functional variants that impair regulated bicarbonate permeation and increase risk for pancreatitis but not for cystic fibrosis. *PLoS Genet* 2014;10:e1004376.
14. Lee MG, Ohana E, Park HW, Yang D, Muallem S. Molecular mechanism of pancreatic and salivary gland fluid and HCO_3^- Secretion. *Physiol Rev* 2012;92:39-74.
15. Roos A, Boron WF. Intracellular pH. *Physiol Rev* 1981;61:296-434.
16. Lee MG, Muallem S. Physiology of duct cell secretion. In: Beger H, Buchler M, Kozarek R, Lerch M, Neoptolemos J, Warshaw A, Whitcomb D, Shiratori K, editors. *Pancreas: An Integrated Textbook of Basic Science, Medicine, and Surgery*. Oxford, U.K.: Blackwell Publishing; 2008. p.78-90.
17. Hatefi Y, Hanstein WG. Solubilization of particulate proteins and nonelectrolytes by chaotropic agents. *Proc Natl Acad Sci U S A* 1969;62:1129-36.
18. Quinton PM. Role of epithelial HCO_3^- transport in mucin secretion: lessons from cystic fibrosis. *Am J Physiol Cell Physiol* 2010;299:C1222-33.
19. Quinton PM. The neglected ion: HCO_3^- . *Nat Med* 2001;7:292-3.
20. Quinton PM. Cystic fibrosis: impaired bicarbonate secretion and mucoviscidosis. *Lancet* 2008;372:415-7.
21. Wang XF, Zhou CX, Shi QX, Yuan YY, Yu MK, Ajonuma LC, et al. Involvement of CFTR in uterine bicarbonate secretion and the fertilizing capacity of sperm. *Nat Cell Biol* 2003;5:902-6.

22. Gee HY, Noh SH, Tang BL, Kim KH, Lee MG. Rescue of $\Delta F508$ -CFTR trafficking via a GRASP-dependent unconventional secretion pathway. *Cell* 2011;146:746-60.
23. Johansen PG, Anderson CM, Hadorn B. Cystic fibrosis of the pancreas. A generalised disturbance of water and electrolyte movement in exocrine tissues. *Lancet* 1968;1:455-60.
24. Staley KJ, Soldo BL, Proctor WR. Ionic mechanisms of neuronal excitation by inhibitory GABAA receptors. *Science* 1995;269:977-81.
25. Ben-Ari Y, Gaiarsa JL, Tyzio R, Khazipov R. GABA: a pioneer transmitter that excites immature neurons and generates primitive oscillations. *Physiol Rev* 2007;87:1215-84.
26. Jun I, Cheng MH, Sim E, Jung J, Suh BL, Kim Y, et al. Pore dilatation increases the bicarbonate permeability of CFTR, ANO1 and glycine receptor anion channels. *J Physiol* 2016 594:2929-55.
27. Cohen BN, Labarca C, Davidson N, Lester HA. Mutations in M2 alter the selectivity of the mouse nicotinic acetylcholine receptor for organic and alkali metal cations. *J Gen Physiol* 1992;100:373-400.
28. Dwyer TM, Adams DJ, Hille B. The permeability of the endplate channel to organic cations in frog muscle. *J Gen Physiol* 1980;75:469-92.
29. Klauda JB, Venable RM, Freites JA, O'Connor JW, Tobias DJ, Mondragon-Ramirez C, et al. Update of the CHARMM all-atom additive force field for lipids: validation on six lipid types. *J Phys Chem B* 2010;114:7830-43.
30. MacKerell AD, Bashford D, Bellott M, Dunbrack RL, Evanseck JD, Field MJ, et al. All-atom empirical potential for molecular modeling and dynamics studies of proteins. *J Phys Chem B* 1998;102:3586-616.
31. MacKerell AD, Jr., Feig M, Brooks CL, 3rd. Improved treatment of the protein backbone in empirical force fields. *J Am Chem Soc* 2004;126:698-9.

32. Phillips JC, Braun R, Wang W, Gumbart J, Tajkhorshid E, Villa E, et al. Scalable molecular dynamics with NAMD. *J Comput Chem* 2005;26:1781-802.
33. Darden T, York D, Pedersen L. Particle Mesh Ewald - an N.Log(N) Method for Ewald Sums in Large Systems. *J Chem Phys* 1993;98:10089-92.
34. Smart OS, Neduvélil JG, Wang X, Wallace BA, Sansom MS. HOLE: a program for the analysis of the pore dimensions of ion channel structural models. *J Mol Graph* 1996;14:354-60, 76.
35. Vanommeslaeghe K, Hatcher E, Acharya C, Kundu S, Zhong S, Shim J, et al. CHARMM general force field: A force field for drug-like molecules compatible with the CHARMM all-atom additive biological force fields. *J Comput Chem* 2010;31:671-90.
36. Hoover W. Canonical dynamics: equilibrium phase-space distributions. *Phys. Rev. A.* 1985;31:1695-7.
37. Nosé S. A Unified formulation of the constant-temperature molecular-dynamics methods. *J Chem Phys* 1984;81:511-9.
38. Chipot C, Hénin J. Exploring the free-energy landscape of a short peptide using an average force. *J Chem Phys* 2005;123: 244906.
39. Cheng MH, Coalson RD. Energetics and ion permeation characteristics in a glutamate-gated chloride (GluCl) receptor channel. *J Phys Chem B* 2012;116:13637-43.
40. Cheng MH, Coalson RD, Tang P. Molecular dynamics and Brownian dynamics investigation of ion permeation and anesthetic halothane effects on a proton-gated ion channel *J Am Chem Soc* 2010;132(46):16442-9.
41. Lee J, Woo J, Favorov OV, Tommerdahl M, Lee CJ, Whitsel BL. Columnar distribution of activity dependent gabaergic depolarization in sensorimotor cortical neurons. *Mol Brain* 2012;5:33.
42. Mennucci B, Tomasi J, Cammi R, Cheeseman JR, Frisch MJ, Devlin FJ, et al. Polarizable continuum model (PCM) calculations of solvent

- effects on optical rotations of chiral molecules. *J Phys Chem A* 2002;106:6102-13.
43. Tomasi J, Mennucci B, Cammi R. Quantum mechanical continuum solvation models. *Chem Rev* 2005;105:2999-3093.
 44. Heads JA, Hawthorne RL, Lynagh T, Lynch JW. Structure-activity analysis of ginkgolide binding in the glycine receptor pore. *J Neurochem* 2008;105:1418-27.
 45. Wieczorek G, Zielenkiewicz P. DeltaF508 mutation increases conformational flexibility of CFTR protein. *J Cyst Fibros* 2008;7:295-300.
 46. Caputo A, Caci E, Ferrera L, Pedemonte N, Barsanti C, Sondo E, et al. TMEM16A, a membrane protein associated with calcium-dependent chloride channel activity. *Science* 2008;322:590-4.
 47. Schroeder BC, Cheng T, Jan YN, Jan LY. Expression cloning of TMEM16A as a calcium-activated chloride channel subunit. *Cell* 2008;134:1019-29.
 48. Yang YD, Cho H, Koo JY, Tak MH, Cho Y, Shim WS, et al. TMEM16A confers receptor-activated calcium-dependent chloride conductance. *Nature* 2008;455:1210-5.
 49. Lynch JW. Molecular structure and function of the glycine receptor chloride channel. *Physiol Rev* 2004;84:1051-95.
 50. Hibbs RE, Gouaux E. Principles of activation and permeation in an anion-selective Cys-loop receptor. *Nature* 2011;474:54-60.
 51. Pezzulo AA, Tang XX, Hoegger MJ, Alaiwa MH, Ramachandran S, Moninger TO, et al. Reduced airway surface pH impairs bacterial killing in the porcine cystic fibrosis lung. *Nature* 2012;487:109-13.
 52. Hubner CA, Holthoff K. Anion transport and GABA signaling. *Front Cell Neurosci* 2013;7:177.
 53. Chung MK, Guler AD, Caterina MJ. TRPV1 shows dynamic ionic selectivity during agonist stimulation. *Nat Neurosci* 2008;11:555-64.

54. Kane Dickson V, Pedi L, Long SB. Structure and insights into the function of a Ca^{2+} -activated Cl^- channel. *Nature* 2014;516:213-8.
55. Dutzler R, Campbell EB, Cadene M, Chait BT, MacKinnon R. X-ray structure of a CLC chloride channel at 3.0 Å reveals the molecular basis of anion selectivity. *Nature* 2002;415:287-94.
56. Eisenman G, Horn R. Ionic selectivity revisited: the role of kinetic and equilibrium processes in ion permeation through channels. *J Membr Biol* 1983;76:197-225.
57. Lim HH, Stockbridge RB, Miller C. Fluoride-dependent interruption of the transport cycle of a CLC Cl^-/H^+ antiporter. *Nat Chem Biol* 2013;9:721-5.

ABSTRACT (IN KOREAN)

음이온채널에서의 이온선택성 동적 변화의 기전

<지도교수 이민구>

연세대학교 대학원 의과학과

전익현

음이온채널을 통한 이온의 수송은 우리 몸에서 아주 중요한 역할을 하고 있다. 하지만 음이온 채널이 이온선택성을 어떻게 유지하고 또한 어떤 기전에 의해 조절되는 지에 대한 연구는 많이 부족하다. 따라서 본 연구를 통해 열역학적 수화 에너지와 이온의 크기에 따른 선별력이 동시에 작용하여 음이온통로의 이온선택성을 결정할 수 있는 것을 확인 하였다. WNK1/SPAK 인산화 효소에 의한 CFTR 의 중탄산염 투과도 증가가 일어날 때 유전상수의 증가와 이온 통로의 확장이 동시에 발생한다. 또한 ANO1/TMEM16A 에서도 세포 내 고농도 칼슘에 의한 중탄산염 투과도 증가가 발생할 때 같은 현상이 일어남을 확인 하였다. 글리신 수용체의 프롤린-2' 결손 돌연변이가 이온 통로의 확장, 중탄산염 투과도 증가, 유전율의 상승을 유발한다. 분자동역학적 모의실험을 통하여 이온 통로의 확장이 이온 크기에 따른 선별력 뿐 아니라 이온 채널 내부의 이온의 선택성 결정 심사부위의 물

분자 점유량을 높여 이온의 탈수화 에너지를 동시에 조절하는 것을 확인 하였다. 가바 수용체에 고농도의 가바를 적용하였을 때 음이온 선택성이 동적으로 조절되고, 이러한 현상은 감각 운동 피질의 피라미드 뉴런에서 가바에 의한 활성 전위 생성에 필수적인 요소임이 확인 되었다. 이러한 열역학적 수화에너지와 이온 크기에 따른 선별력을 종합하여 새로운 음이온 선택성 모형화를 시행하였다. 특히 세포 내 자극을 통해 이온선택성이 동적으로 조절되는데 있어 이온 통로의 구멍 크기가 변화하는 것이 중요하다는 것을 밝혔다. CFTR, ANO1/TMEM16A, 글리신 수용체, 가바 수용체 같은 다양한 이온 채널에서 이온 통로 크기의 증가로 인해 중탄산염의 투과도가 증가하는 현상을 발견하였는데 이것은 이온 크기에 따른 선별 및 이온의 수화에너지를 조절하여 일어남을 규명하였다. 또한 이러한 중탄산염의 동적인 투과도 증가가 CFTR 을 통한 중탄산염의 분비나 가바수용체를 통한 신경 활성등의 많은 생리학적 그리고 병태생리학적인 과정에 관련이 있다는 것에 대한 증거를 제시하였다.

핵심되는 말: 음이온선택성, CFTR, ANO1/TMEM16A, 글리신 수용체, 가바 수용체, 중탄산염, 유전율, 이온 통로 크기

PUBLICATION LIST

1. Gee HY*, **Jun I***, Braun DA, Lawson JA, Halbritter J, Shril S, et al. Mutations in SLC26A1 cause nephrolithiasis. *Am J Hum Genet* 2016;98(6):1228-34. (* equal contribution)
2. **Jun I**, Cheng MH, Sim E, Jung J, Suh BL, Kim Y, et al. Pore dilation increases the bicarbonate permeability of CFTR, ANO1, and glycine receptor anion channels. *J Physiol* 2016;594(11):2929-55.
3. Lee CS*, **Jun I***, Choi SI, Lee JH, Lee MG, Lee SC, et al. A novel BEST1 mutation in autosomal recessive bestrophinopathy. *Invest Ophthalmol Vis Sci*. 2015;56(13):8141-50. (* equal contribution)
4. Kim HJ*, **Jun I***, Yoon JS, Jung J, Kim YK, Kim WK, et al. Selective serotonin reuptake inhibitors facilitate ANO6 (TMEM16F) current activation and phosphatidylserine exposure. *Pflugers Arch – Eur J Physiol*. 2015;467(11):2243-56. (* equal contribution)
5. **Jun I**, Choi YJ, Kim EK, Seo KY, Kim TI. (2012) Internal spherical aberration by ray tracing-type aberrometry in multifocal pseudophakic eyes. *Eye (Lond)*. 2012;26(9):1243-8